An analysis of sedimentary archaea to characterize chemoorganoautotrophic metabolism at cold methane seeps

A thesis presented by

Kemi Ashing-Giwa

to the Faculty of the Department of

Organismic & Evolutionary Biology

in partial fulfillment of the requirements

for the degree with honors

of Bachelor of Arts

Harvard University

Cambridge, Massachusetts

March, 2022

Honor Code

In submitting this thesis to the Department of Organismic & Evolutionary Biology in partial fulfillment of the requirements for the degree with honors of Bachelor of Arts, I affirm my awareness of the standards of the Harvard College Honor Code.

Name: Kemi Ashing-Giwa

Signature: 

The Harvard College Honor Code

Members of the Harvard College community commit themselves to producing academic work of integrity—that is, work that adheres to the scholarly and intellectual standards of accurate attribution of sources, appropriate collection and use of data, and transparent acknowledgement of the contribution of others to their ideas, discoveries, interpretations, and conclusions.

Cheating on exams or problem sets, plagiarizing or misrepresenting the ideas or language of someone else as one's own, falsifying data, or any other instance of academic dishonesty violates the standards of our community, as well as the standards of the wider world of learning and affairs.

Abstract

Knowledge of the environmental conditions that can develop and support life on our own planet is the best basis available for identifying potential extraterrestrial habitats. The goal of this study was to examine marine archaeal communities at a cold methane seep by analyzing the carbon isotopic composition of archaeal tetraether lipid biomarkers, GDGTs. Cold methane seeps are of great interest because they are a terrestrial analog for possible environments on moons with subsurface oceans, such as Europa and Enceladus. The major objectives of this project were to (I) determine if these archaeal groups are predominantly taking up carbon from autotrophic sources in the water column or from sedimentary methanotrophic sources; (II) quantify the actual contribution of archaeal methanotrophic metabolism; and (III) explore how GDGT distributions at cold methane seeps differ from other environments.

After lipid extraction, specific GDGTs were separated via high-performance liquid chromatography. Carbon isotopic composition of the compounds was derived using a spooling-wire micro-combustion and isotope ratio mass spectrometer. (I, II) Overall, the archaeal groups appeared to be taking up more carbon from autotrophic water column sources than from sedimentary methanotrophic sources. As anticipated, the fractional contribution of the former was highest at the coretop samples and decreased with depth. (III) Chromatography showing GDGT distribution at the seep is consistent with the chromatography of a typical cold marine environment, and displays clear differences from typical warm marine and methane-impacted environments. Coupled with the carbon isotope results, the collected relative abundance and chromatographic data support the theory of a possible active Thaumarchaeota community at the uppermost sample layer. Ultimately, this project presents several insights into an astrobiologically-intriguing microbial ecosystem, and offers a number of avenues for further exploration.

Acknowledgements

I would like to express my deepest gratitude to my advisors Professor Ann Pearson and Professor Peter Girguis, my mentors Katherine Keller and Isabel Baker, the Pearson and Girguis groups, and the Departments of Earth & Planetary Sciences and Organismic & Evolutionary Biology.

None of this work would have been possible without Katherine and Isabel, who provided incredible mentorship throughout the entire project. Susie Carter, Dr. Samuel Phelps, Ana Gonzalez-Nayeck, and Daianne Höfig were also extraordinarily generous with their time, whether they were helping me troubleshoot equipment issues or teaching me a new technique.

I would also like to thank the Origins of Life Initiative, the Earth & Planetary Sciences Department, and the Office of Undergraduate Research & Fellowships for funding this project.

And, of course, thank you to my friends and family, who were with me every step of the way.

Attribution of Work

Isabel Baker collected both cores studied from Astoria Canyon. Isabel also created the diagram that was used as the basis for Fig. 4.

Sample processing was carried out under the supervision of Katherine Keller. Before I began work, she freeze-dried Samples 1 and 3. In addition to several rounds of flow injection analysis, she carried out normal phase high-performance liquid chromatography on Samples 7, 9, and 11. With the aid of Johnston Lab graduate student Daianne Höfig, she also collected the triple quadrupole mass spectrometry and chromatographic data used to make, respectively, Fig. 10-12 and Fig. 14-16.

Spooling-wire micro-combustion and isotope ratio mass spectrometry was conducted with Katherine and Dr. Samuel Phelps.

When searching the literature for end members to calculate fractional contributions, I used values found by Katherine as a guide to ensure reasonable ranges. She also lended invaluable expertise and gave extensive feedback during the interpretation of results.

Table of Contents

List of Figures, Tables, and Equations

Figures

Tables

Equations

Abbreviations

1. ANME: anaerobic methanotrophic (archaea)
2. AOM: anaerobic oxidation of methane
3. APCI-MS: atmospheric pressure chemical ionization-mass spectrometry
4. Cren and Cren': Crenarchaeol and Crenarchaeol-regioisomer
5. DCM: dichloromethane
6. EtOAc: ethyl acetate
7. FIA: flow injection analysis
8. GDGT: glycerol dialkyl glycerol tetraethers
9. HPLC: high-performance liquid chromatography
    - 9.1. NP-HPLC: normal phase high-performance liquid chromatography
    - 9.2. RP-HPLC: reversed phase high-performance liquid chromatography
10. Hx: hexane
11. IRMS: isotope ratio mass spectrometry
    - 11.1. GC-IRMS: gas chromatography isotope ratio mass spectrometry
    - 11.2. SWiM-IRMS: spooling-wire micro-combustion device and isotope ratio mass spectrometry
12. MARS: microwave assisted extraction system
13. MeOH: methanol
14. MI: methane index
15. QQQ-MS: triple quadrupole mass spectrometry
16. RI: ring index
17. S#: Sample #

18. SST: sea surface temperature

19. TIC: total ion count

20. TLE: total lipid extract

    20.1. TLE-TE: transesterified total lipid extracts

Introduction

Of the three domains of life on our planet, Archaea remain the least understood (Woese et al.,1978; Allers and Mevarech, 2005; Valentine, 2007). The first-characterized archaea were isolated from environments distinguished by high temperature, acidity, salinity, and/or strict anoxia (Rothschild and Mancinelli, 2001; Valentine, 2007 and references within). These discoveries led to the hypothesis that these life forms require extreme conditions to survive (Rothschild and Mancinelli, 2001; Valentine, 2007 and references within). However, recent investigations of archaeal phylogenetic diversity have shown that these organisms are abundant in a vast array of habitats across Earth's biospheres (DeLong, 1992; Fuhrman et al., 1992; Chaban et al., 2006; Valentine, 2007).

Extremophiles, of which a high proportion are archaea (Cavicchioli, 2002), are of great interest as potential model organisms for answering fascinating questions about life in harsh environments and the capacity for life to react to its surroundings. The improved knowledge of Archaean habitats has expanded the quantity and variety of extraterrestrial locations that may be targeted for exploration (Gulick, 2001; Cavicchioli, 2002).

Contemporary studies of Archaea and other extremophiles have resulted in a better understanding of their cellular evolution (Cavicchioli, 2002); the identification of new biomarkers (Blake et al., 2001; Cavicchioli, 2002); insight into the capacity of microorganisms to survive global extinction events; and have bolstered techniques in the handling, study, and detection of possible life in environmental samples from Mars and meteorites (Zoltov et al., 2000; Gulick, 2001; Cavicchioli, 2002). Archaea are thus invaluable tools toward exploring the origin of life on our own planet.

The aforementioned origins of life inquiries are of great interest to both the Pearson and Girguis labs, the host labs for this project. Investigating the mechanisms by which the earliest forms of life (which were undoubtedly microbial in nature) survived the extreme conditions on a young Earth—and how they currently survive their wide range of environments—is a major focus of astrobiology. Such studies have the potential to reveal the possible appearance and structure of extraterrestrial life (Cavicchioli, 2002).

Since the technology needed to study exoplanets in detail is still in its infancy, knowledge of the environmental conditions that can develop and support life on our own planet is the only basis available for identifying potential extraterrestrial habitats. Such knowledge is especially important given that NASA (the National Aeronautics and Space Administration) and ESA (the European Space Agency) are currently finalizing mission plans to study the potential habitability of ocean worlds in our own solar system (Gudipati et al., 2020). This proposed study will examine a cold seep, a terrestrial analog for extraterrestrial environments which may exist on moons with subsurface oceans, such as Europa and Enceladus (satellites of Jupiter and Saturn, respectively) (Russell et al., 2017).

Cold seeps are areas on the ocean floor where hydrogen sulfide and hydrocarbon-rich gases like methane percolate through underlying rock and sediment layers and emerge at the ocean bottom (Foucher et al., 2009). These cold seeps harbor rich ecosystems based on microbes that use methane as their energy source (Foucher et al., 2009; Russell et al., 2017). The same chemicals that nourish seafloor life around cold methane seeps might also sustain life near undersea habitats on exoplanets (Russell et al., 2017).

Of the biomarkers that can be studied with current technology, lipids make excellent candidates as they are typically very well preserved (Parenteau et al., 2014; Wilhelm et al.,

2017). Furthermore, their uniquely-produced structures can be readily classified and assigned to a taxon (Ding et al., 2017; Kurth et al., 2019). GDGTs (glycerol dialkyl glycerol tetraethers), are a class of organic compounds present in the cell membranes of specific microbial groups, making them an excellent biomarker diagnostic of certain phyla (Pearson et al., 2016).

While mesophilic (i.e., nonthermophilic) eukaryotes and bacteria typically possess bilayers with ester bonds, GDGTs have ether bonds and form monolayers that are nearly impermeable to ions and protons (Schouten et al., 2013). It is thought that these features play a significant role in stabilizing hyperthermophilic membranes at low pHs and high temperatures (Schouten et al., 2000 and 2013). Based on this idea, it is probable that GDGTs existed primarily at hydrothermal vents, in hot springs, and other extreme environments. However, various studies of environmental samples from mesophilic environments including soils, lakes, and oceans have demonstrated that GDGTs are common, structurally diverse, and produced by some bacteria as well as archaea (Schouten et al., 2000 and 2013; Weijers et al., 2006).

GDGTs are composed of two or more units of hydrocarbons, with each unit consisting of five carbon atoms arranged in a specific pattern. GDGTs are grouped into two major classifications based on the structures of their carbon skeletons: isoprenoid and branched (Schouten et al., 2013). This project is concerned with the former.

Depending on the number of cyclopentane rings, isoprenoid GDGTs are numbered 0-8 except for crenarchaeol (Cren), which has four cyclopentane rings in addition to a cyclohexane group (Schouten et al., 2013). The mass-to-charge ratios (m/z) of the GDGTs of interest for this project are as follows: 1302 m/z for GDGT-0, 1300 m/z for GDGT-1, 1298 m/z for GDGT-2,

1296 m/z for GDGT-3, 1292 m/z for Crenarchaeol (Cren), and 1292' m/z for Crenarchaeol regioisomer[1] (Cren') (Tierney and Tingley, 2015).

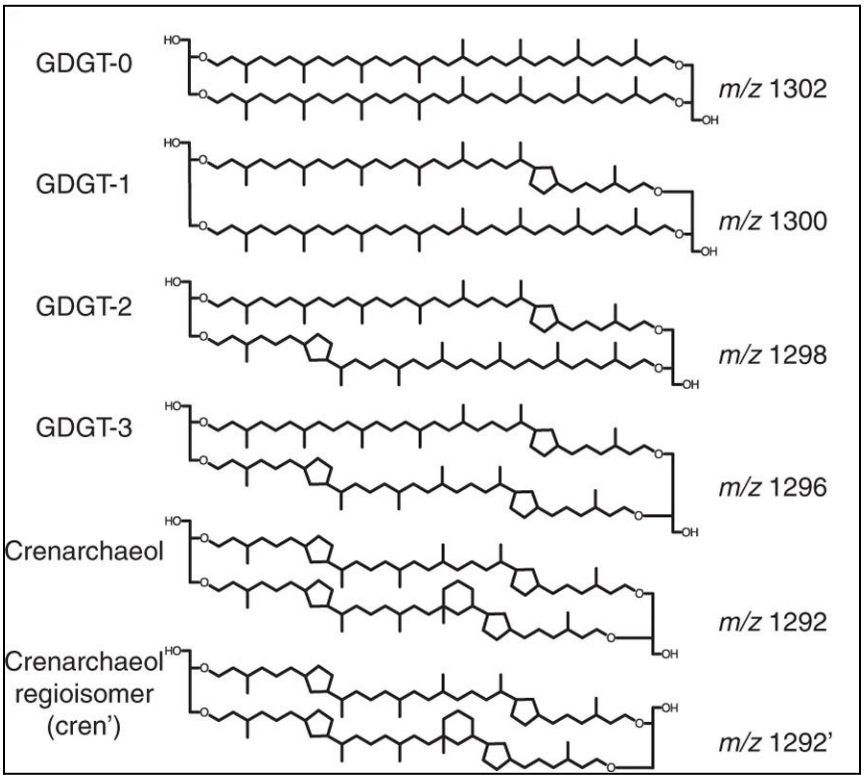

Fig. 1: The molecular structures of GDGTs (Tierney and Tingley, 2015).

The distribution and composition of the cyclopentane rings is thought to be determined by different environmental factors, particularly pH and temperature; generally, the greater the stress, the greater the number of cyclopentane rings (De Rosa et al., 1986; Macalady et al., 2004; Boyd et al., 2010; Pearson and Ingalls, 2013). Resource starvation, ionic strength, and pressure are other environmental stressors that can have an impact (Valentine, 2007; Pearson and Ingalls, 2013 and references therein). In marine settings (but not necessarily generally), GDGT-0 and

[1] Crenarchaeol regioisomer possesses the same functional groups as Crenarchaeol, but they are attached at different positions.

Crenarchaeol are the most abundant, while GDGT-1, GDGT-2, and GDGT-3 are "minors" (i.e., they are much rarer) (Besseling et al. 2020).

When these GDGTs are observed in archaea, it is often difficult to determine certain key characteristics about the specimen's origin, such as whether it was methane-producing (methanogenic), methane-consuming (methanotrophic), or had an entirely different metabolism—as is the case for most archaea (Moreira et al., 1998; Lloyd et al., 2011; Pohlman, 2011; Francis et al., 2005).

Carbon isotope ratios ($\delta^{13}C$) are an extremely useful measurement by which to investigate metabolism (Yuen, et al., 1984; Silvera et al., 2010). Methanotrophs take up methane and oxidize it with sulfate (SO_4), converting it to bicarbonate to gain energy. The reaction is as follows: $CH_4 + SO_4^{2-} \rightarrow HCO3^- + HS^- + H_2O$ (Reeburgh, 1976; Knittel et al., 2009). Methane production is isotopically light due to the large isotopic fractionation associated with enzymatic carbon fixation[2]. The low $^{13}C/^{12}C$ ratio that results generates a unique signal. GDGTs made with this isotopically-light methane reflect their carbon sources in their $\delta^{13}C$ values. Methanogenesis, on the other hand, is the generation of methane from carbon dioxide. The reaction is as follows for a carbon dioxide (bicarbonate, HCO_3^-) substrate: $4H_2 + HCO3^- + H+ \rightarrow CH_4 + 3H_2O$ (Buan, 2018). Similarly, there is discrimination between light and heavy isotopes; GDGTs whose carbon source is HCO_3^- have a high high $\delta^{13}C$. These processes are especially important in that methanotrophy and methanogenesis[3] respectively produce and take up bicarbonate, which allows the oceans to maintain a stable pH (e.g.: Kheshgi, 1995; Kump et al., 2009; Gao, 2020).

[2] Kinetic isotope effects: heavier isotopes move more slowly through reactions, due to a need for greater energetic input to reach the transition state.

[3] While this project was concerned primarily with the distinction between methanotrophically- and autotrophically- sourced GDGTs, methanogenesis is still worthy of mention given its importance in marine settings.

Despite the existence of many benthic groups, it is thought that planktonic, ammonia-oxidizing Thaumarchaeota are the dominant producers of GDGTs in the water column, and are thus the source of most of the archaeal GDGTs that settle into marine sediments[4] (Pearson et al., 2016). These archaea live in a specific zone of the ocean with consistent carbon distribution, and GDGTs made from a single source with a single metabolism should generate similar carbon isotope ratios. Thus, when archaeal lipids are sampled from the water column, they are expected to have identical $\delta^{13}C$ values. However, in reality, the carbon isotope ratios differ drastically in areas where methane is actively seeping into the water column, specifically in places where archaea are likely consuming methane (Elvert et al., 2000; Lloyd et al., 2011; Elling et al., 2019)—such as the site studied here.

As a step toward probing the metabolisms at such sites, sediment samples were collected from an active cold methane seep environment at Astoria Canyon, Cascadia Margin and analyzed using an array of geochemical methods. The major objectives of this study were to (I) determine if these archaeal groups are predominantly taking up carbon from autotrophic sources in the water column or from in-situ methanotrophic sedimentary sources; (II) quantify the actual contribution of archaeal methanotrophic metabolism; and (III) explore how GDGT distributions in complex systems like a cold methane seep differ from other sites.

The findings of this exploratory project could also allow for the more accurate classification of similar isotope signals in samples of past geological records. The ability to distinguish novel biomarker scenarios can significantly inform analyses of contemporary organic seep environments, as well as ancient and extraterrestrial environments.

[4] There is, however, ongoing conversation concerning potential additional sources (Lincoln et al., 2014; Pearson et al., 2016).

Materials and Methods

I. Samples

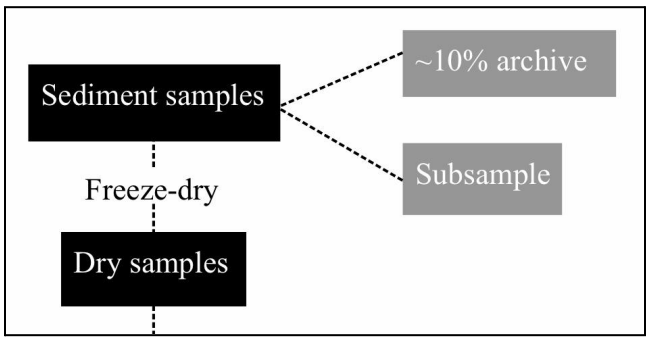

Fig. 2: Sample preparation flowchart.

Archaeal GDGTs are ubiquitous in marine sediments (Pearson et al., 2016). Sediment push cores[5] were collected in the summer of 2018 from several actively-seeping methane sites along the Cascadia Margin off the coast of Washington and Oregon, two of which were taken at Astoria Canyon (latitude: 46° 13.289, longitude: -124° 39.409) (Fig. 3). All samples were processed the next day and were later stored in a -20 °C freezer.

[5] A core tube is pushed down into sediment using the manipulator arm of a remotely operated vehicle. One-way valves allow water to exit as sediment fills the tube.

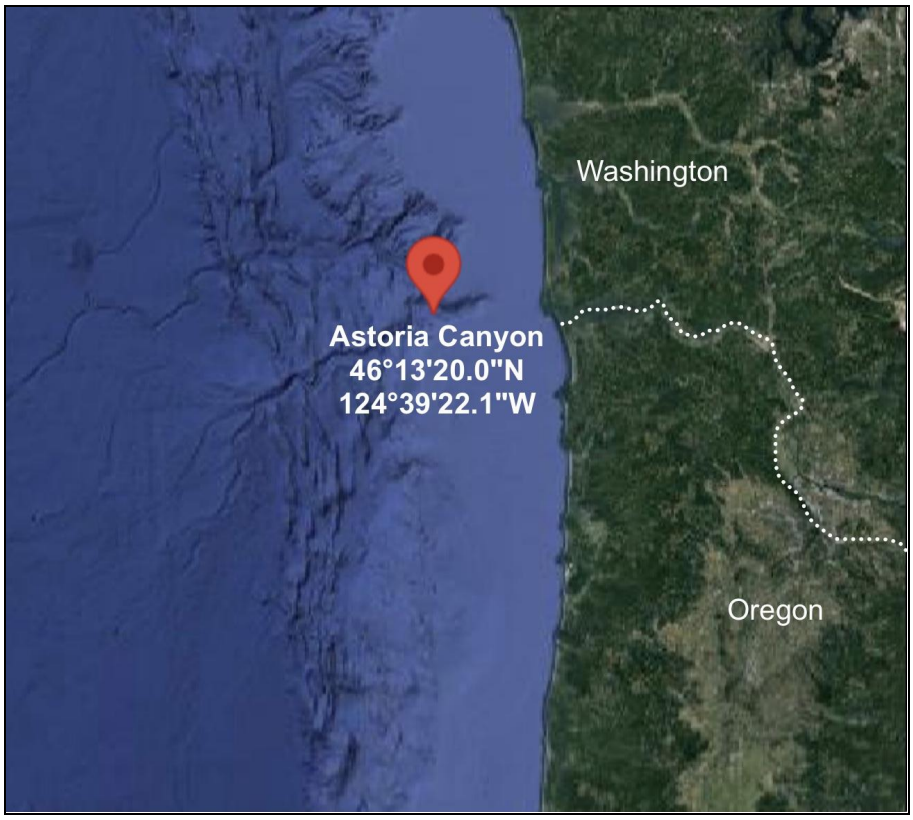

Fig. 3: Location of the Astoria Canyon cold methane seep.

Core 2 was taken from directly within an actively bubbling methane plume and Core 1 was taken approximately 20 meters away (Fig. 4).

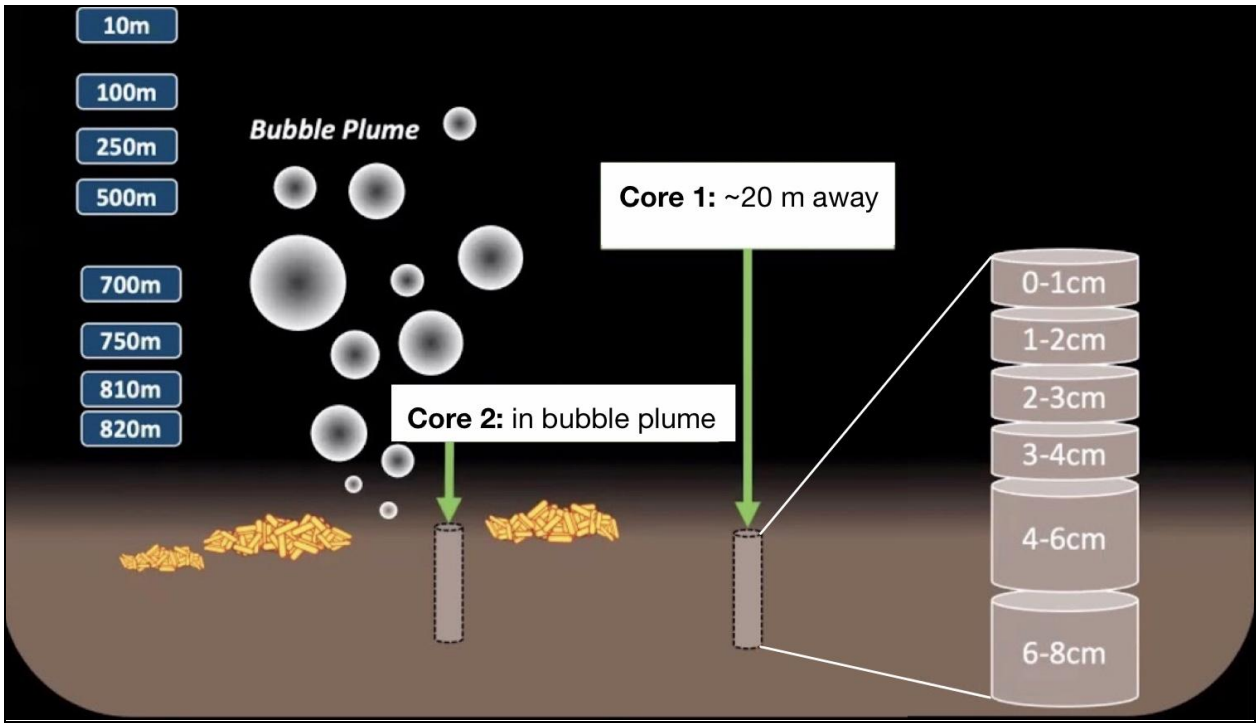

Fig. 4: Water column and sediment core-sampling scheme (adapted from a figure by Isabel Baker). Microbial mats are illustrated in yellow, sample water depths are indicated in the blue boxes to the left, and core slices are represented in the brown cylindrical disks to the right.

Both cores were taken at a water depth of 494 meters. The Core 1 samples were numbered 1, 3, 4, and 5; the Core 2 samples were numbered 7, 9, 10, and 11. Sample information is presented in Table 1. All samples were processed the day after collection; they were prepared for fluorescence *in situ* hybridization, scanning electron microscopy, and 16S rRNA sequencing analysis.

Table 1: Sample information for Core 1 (A) and Core 2 (B).

A

Sample ID	**Distance from plume (m)**	**Depth interval (cm)**
S1	20	0-1
S3	20	2-3
S4	20	3-4
S5	20	4-6

B

Sample ID	**Distance from plume (m)**	**Depth interval (cm)**
S7	0	0-1
S9	0	2-3
S10	0	3-4
S11	0	4-6

II. Extraction and Processing

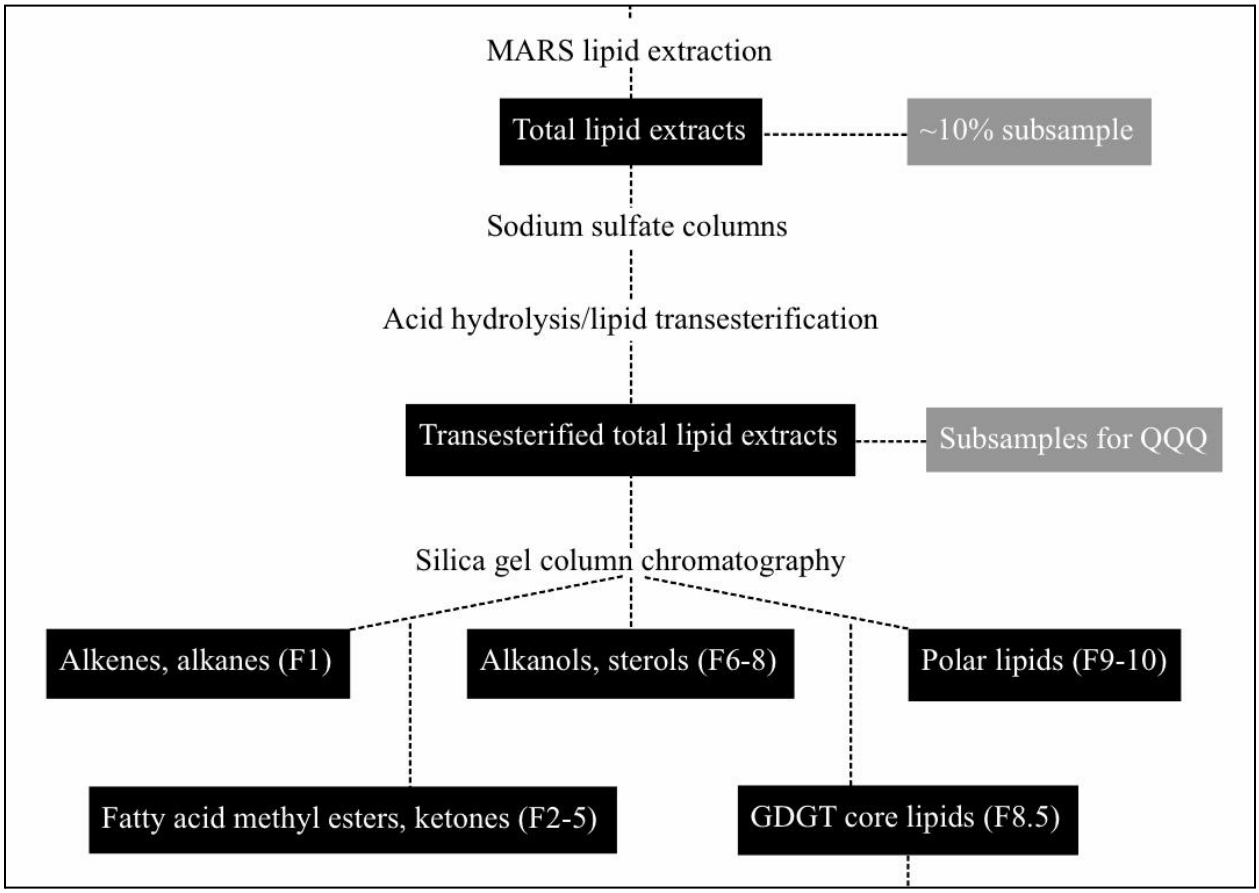

Fig. 5: Lipid extraction and processing flowchart.

I extracted archaeal lipids from the eight sediment samples representing the two cores, and set aside subsamples for future genetic analysis. After taking 10% archives for future work, sediment samples were first freeze-dried with dry ice for 1-2 days, depending on the mass and water content. Samples were then homogenized with a mortar and pestle, transferred into clean containers, and stored in a lab freezer at -20 C.

Total lipid extracts (TLEs) were obtained using a microwave assisted extraction system (MARS) and using a four-part extraction method developed by the Pearson Lab. Samples were

transferred to Teflon cells and mixed with a 50:50 DCM:MeOH (dichloromethane[6]:methanol[7]) solvent mixture. The cells were loaded into the MARS and treated with the appropriate method. After allowing the cells to cool, the samples were centrifuged for eight minutes. The liquid was then decanted into a glass Turbovap flask. The aforementioned steps were then repeated with 90:10 DCM:MeOH and 100% DCM solvent mixtures. After this step, the samples underwent three rounds of DCM rinses. The TLEs were then dried down under clean streams of N_2 via a Turbovap before being run through two to three rounds of sodium sulfate (Na_2SO_4) columns to remove impurities and remaining water. Semi-quantitative 10% archives were taken for triple quadrupole mass spectrometry (QQQ-MS)[8], and the TLEs were stored in a -20 °C lab freezer.

The next major step was to cleave the head groups of the lipids to obtain core GDGTs (along with bulk organic compounds). Lipid transesterification involved dissolving the samples in 95:5 δ^{13}C-known MeOH:HCl (hydrogen chloride) Ultrex solution, and then heating the mixture at 70 °C for four hours within a fume hood. The samples were then pipetted into separatory funnels. Each sample vial was rinsed with two rounds of 10 mL of nanopure H_2O and two rounds of 10 mL 9:1 DCM:Hx (hexane[9]), which were then added to the funnel. The mixtures were shaken and the layers were allowed to separate. If an emulsion formed, a 5% NaCl-water mixture was added. For each sample, the bottom organic layer would be drained into a clean Turbovap flask. Sodium sulfate was first added and mixed in to remove residual water before draining, and the extraction step was repeated with at least four more aliquots of the DCM:Hx mixture. The TLE-TEs (transesterified total lipid extracts) were dried down and transferred to clean vials for freezer storage.

---

[6] DCM: a semi-polar solvent also known as methylene chloride; the formula is CH_2Cl_2.
[7] MeOH: a highly polar solvent also known as methyl alcohol; with the formula CH_3OH.
[8] A quadrupole is a pair of metal rods arranged symmetrically about an axis. In QQQ, the third quadrupole can be set to monitor only specific ions.
[9] Hx: a nonpolar solvent with the formula C_6H_{14}.

The third major step was to separate the TLE-TEs over silica (SiO_2) gel columns into five fractions using mixtures of Hx and ethyl acetate (EtOAc)[10]. The samples move through silica based on polarity (e.g., a nonpolar solvent removes nonpolar alkanes and alkenes, while more polar solvent removes GDGTs). The solvent rounds for silica column chromatography were as follows: F1, 100% Hx to collect alkenes and alkanes; F2-5, 10% EtOAc:Hx to collect fatty acid methyl esters and ketones; F6-8, 25% EtOAc:Hx to collect alkanols and sterols; and F8.5, 50% EtOAc:Hx (which were 7.5 mL instead) to collect GDGT core lipids. The final round, F9-10, consisted of one 7.5 mL EtOAc rinse followed by one 7.5 mL MeOH rinse to collect the most polar lipids. The solvent mixtures were drained through the column into glass Turbovap vessels between each round of rinsing. Further MeOH rinses occurred until all the organic matter was visibly removed (i.e., the slurry was colorless). After drying down the separated lipid fractions in the Turbovap to a low volume and transferring them into clean glassware, all the samples were placed in the freezer for safekeeping.

[10] EtOAc: CH_3-COO-CH_2-CH_3, which is often simplified to $C_4H_8O_2$.

III. High-performance Liquid Chromatography

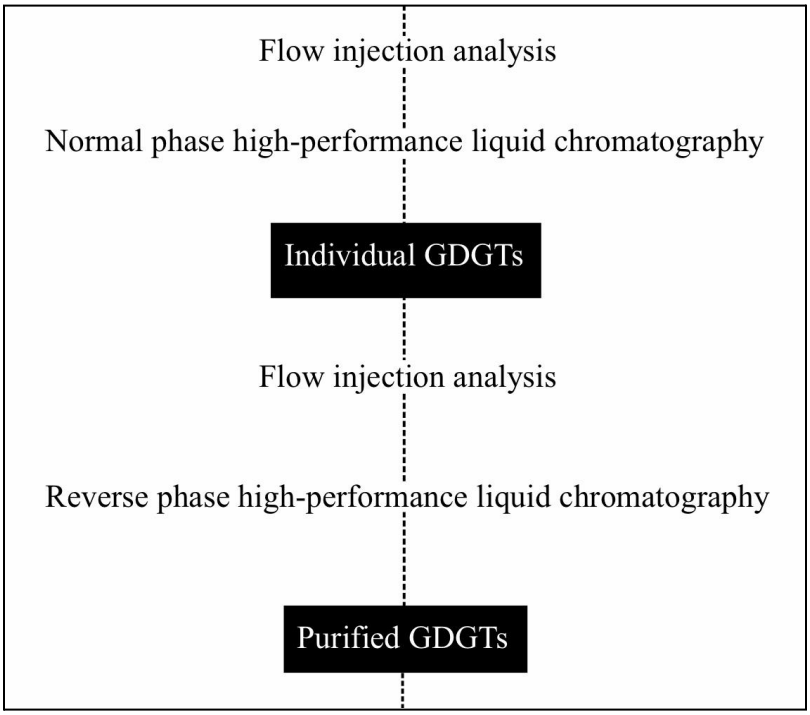

Fig. 6: High-performance liquid chromatography flowchart.

The next step was to perform flow injection analysis (FIA) relative to a dilution series of synthetic C_{46}-GDGT standards, which rendered concentration estimates of the GDGTs. This was followed by normal phase high-performance liquid chromatography (NP-HPLC) to collect individual target GDGTs, and reversed phase HPLC (RP-HPLC) to purify those GDGT fractions by further removing non-target background material (Pearson et al., 2016). During NP-HPLC, the mobile phase is more polar than the stationary phase, so less polar compounds elute first, thereby separating out individual GDGTs by their differences in polarity. The sample (which always remains in liquid form) runs through a ZORBAX NH_2 separation column (4.6 × 250 mm, 5 mm; Agilent Technologies) and has its compounds isocratically[11] separated by mass/charge ratio. The concentration of the mobile phase is 1.35% IPA in Hx; flow rate was 1 ml/min.

[11] The composition of the mobile phase is both constant and uniform.

During RP-HPLC, the stationary phase is more polar than the mobile phase, so more polar compounds elute first, thereby removing non-GDGT substances. Here, the sample runs through a ZORBAX Eclipse XDB-C8 column (4.6 × 150 mm, 5 mm; Agilent Technologies), where the compounds are separated in a gradient. The following program is used following standard methods (e.g.: Ingalls et al., 2006): 100% solvent A (8:2 acetonitrile:water) to 90% A and 10% EtOAc over 4 minutes, to 65% A over 10 minutes, to 31% A over 6 minutes, to 100% EtOAc over 7 minutes. One-minute fractions, thus separated by polarity, were collected and analyzed by FIA.

As a result of ion suppression between samples, the values obtained from FIA were only semi-quantitative (Pearson et al., 2016). However, the estimated concentrations still served to help ensure that the column was not overloaded during HPLC, thereby improving separations. All purifications were limited to 20 micrograms per total GDGT injection, which is less material than previously used per injection in most similar studies outside the Pearson lab (Ingalls et al., 2006; Shah and Pearson, 2007; Shah et al., 2008).

To define compound-specific collection windows for NP-HPLC, a preliminary sample is screened via atmospheric pressure chemical ionization-mass spectrometry (APCI-MS). In RP-HPLC, which is also conducted with a timing run, the GDGTs of interest (from GDGT-0 to Crenarchaeol) elute within a narrow window and are collected in three one-minute time slices: the preceding minute (F1), the GDGT fraction (F2), and the final tailing minute (F3). Each run was standardized to the same reference frame using three sets of standards: C_{46}-GTGT (Huguet et al., 2006); Carolina Margin Crenarchaeol; and Saci-v1, which is derived from the thermoacidophilic archaeon *Sulfolobus acidocaldarius*.

FIA was repeated between rounds of chromatographic purification to keep track of the amounts of each compound, and to ensure the GDGT fractions were separating properly. Purified GDGT fractions were removed from the HPLC, briefly stored in a laminar flow hood, dried under N_2, and dissolved in EtOAc.

IV: Spooling-wire Micro-combustion and Isotope Ratio Mass Spectrometry

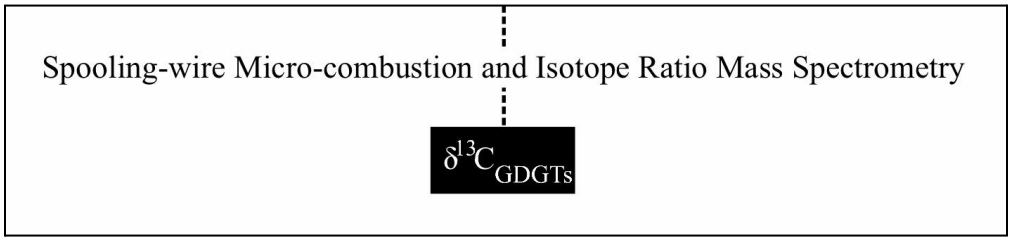

Fig. 7: Spooling-wire micro-combustion device and isotope ratio mass spectrometry flowchart.

Finally, we used a spooling-wire micro-combustion device and isotope ratio mass spectrometry (SWiM-IRMS) to measure the $\delta^{13}C$ values of carbon in the GDGT molecules. The Pearson lab system is similar to that developed by Sessions et al., 2005, with the addition of GDGT-specific modifications: a ceramic combustion reactor with modified gas flow (Mohr et al., 2014), a 950 °C cleaning furnace, and a 900 °C combustion furnace (Pearson et al., 2016).

Conventionally, GDGTs can be cleaved into C_{40}biphytanes for gas chromatography isotope ratio mass spectrometry (GC-IRMS). However, a consequence of this method is the loss of valuable information about the isotopic heterogeneity of GDGTs within a sample (Pearson et al., 2016). This approach may also result in isotopic fractionation corresponding to the ether cleavage, though there is evidence that the effect is insignificant (Pearson et al., 2016).

Nevertheless, in utilizing SWiM, the Pearson Lab is one of the few labs in the world that can measure the entire tetraether structure of GDGTs, which are too large to volatilize whole.

During SWiM-IRMS, 1 microliter of sample is deposited on pre-oxidized nickel wire, which moves horizontally into a combustion furnace. The carbon in the GDGTs is converted into CO_2. The CO_2 is ionized in a Nafion[12] drying tube, within which water molecules are also removed. The analyte enters the IRMS through an open split, whereupon the analyzer of the mass spectrometer separates the CO_2 molecules by mass to charge ratio. The samples are individually analyzed in quintuplicate 30 second intervals.

To ensure the accuracy of the $\delta^{13}C_{GDGT}$ data, a dilution series of the C_{46}-GTGT standard is analyzed with every SWiM-IRMS run. Results from the dilution series are used to apply absolute offset and blank corrections to the raw data, and thereby ensure that $\delta^{13}C$ values are standardized to the same reference frame (Pearson et al., 2016).

[12] Nafion: sulfonated tetrafluoroethylene based fluoropolymer-copolymer; a class of synthetic polymers with ionic properties (Kusoglu and Weber, 2017).

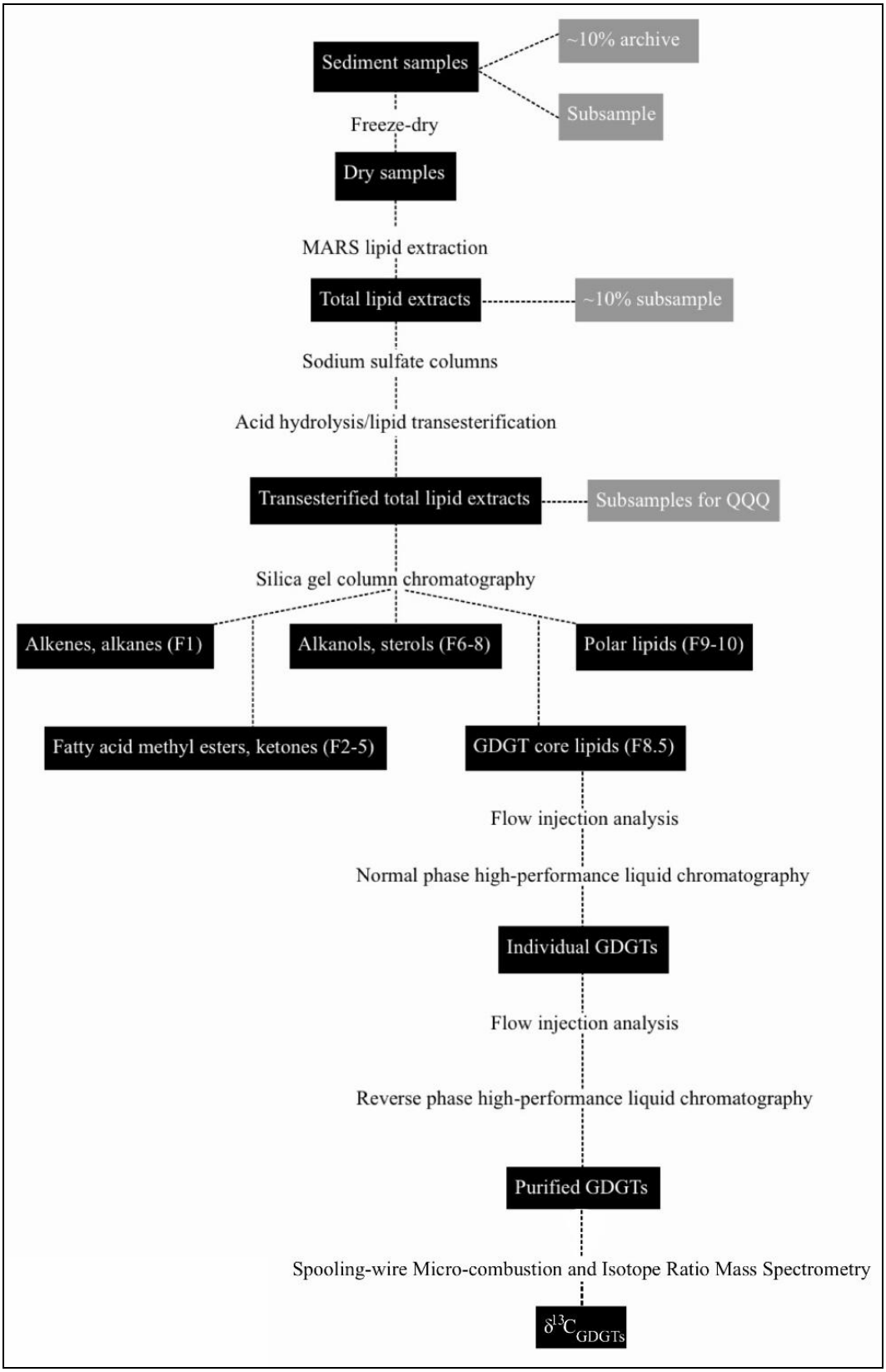

Fig. 8: Complete GDGT analysis flowchart.

Results

The data collected over the course of this project can be categorized as follows: (I) $\delta^{13}C_{GDGT}$ data and validation, (II) relative abundances of GDGTs, (III) ring index values, and (V) chromatography results.

I: $\delta^{13}C_{GDGT}$ Data and Validation

Table 2: $\delta^{13}C_{GDGT}$ values for Core 1

Sample ID (Core 1)	**Compound**	**$\delta^{13}C$ (‰)**	**ST deviation**
S1	GDGT-0	-30.91	0.10
	GDGT-2	-83.71	0.27
	Crenarchaeol	-22.73	0.24
S4	GDGT-0	-48.29	0.22
	GDGT-2	-85.14	0.30
	Crenarchaeol	-23.87	0.06
S5	GDGT-0	-63.31	0.21
	GDGT-1	-73.35	0.21
	GDGT-2	-93.32	0.38
	Crenarchaeol	-25.92	0.13

Table 3: $\delta^{13}C_{GDGT}$ values for Core 2

Sample ID (Core 2)	**Compound**	**δ_{13}C (‰)**	**ST deviation**
S7	GDGT-0	-26.16	0.48
	GDGT-2	-81.00	0.26
	Crenarchaeol	-23.01	0.07
S9	GDGT-0	-34.27	0.27
	GDGT-2	-92.52	0.56
	GDGT-3	-89.81	0.57
	Crenarchaeol	-28.98	0.27
S10	GDGT-0	-35.05	0.14
	GDGT-1	-78.34	0.27
	GDGT-2	-91.61	0.21
	Crenarchaeol	-31.55	0.23
S11	GDGT-0	-36.78	0.20
	GDGT-1	-84.06	0.71
	GDGT-2	-96.46	0.53
	GDGT-3	-94.52	0.98
	Crenarchaeol	-36.44	0.54

F2/F1 ratios describe the amount (μg) of material eluting during the first minute of RP-HPLC (F1) versus the correct fraction for GDGTs (F2). Plots comparing F2/F1 ratios and carbon isotope ratios (see Appendix, Fig. 22) were used to determine the cutoff for viable $\delta^{13}C_{GDGT}$ values. Low ratios indicate that there is a low signal-to-noise ratio. In Core 1, the natural cutoff point was determined to be approximately 5. In Core 1, the S5 Crenarchaeol

sample possesses the lowest F2/F1 value, 4.54 (Fig. 22 A). However, this was determined to be sufficiently high enough to retain based on overall evaluation of the total dataset. This cutoff value is similar to those used in previous work in the Pearson Lab (Pearson et al., 2016). The Core 2 samples all possess sufficiently high F2/F1 values; the S7 GDGT-2 sample possesses the lowest value, 5.65 (Fig. 22 B).

In addition, low purity samples were also removed. Thus, in Core 1, there is only one value for GDGT-1.

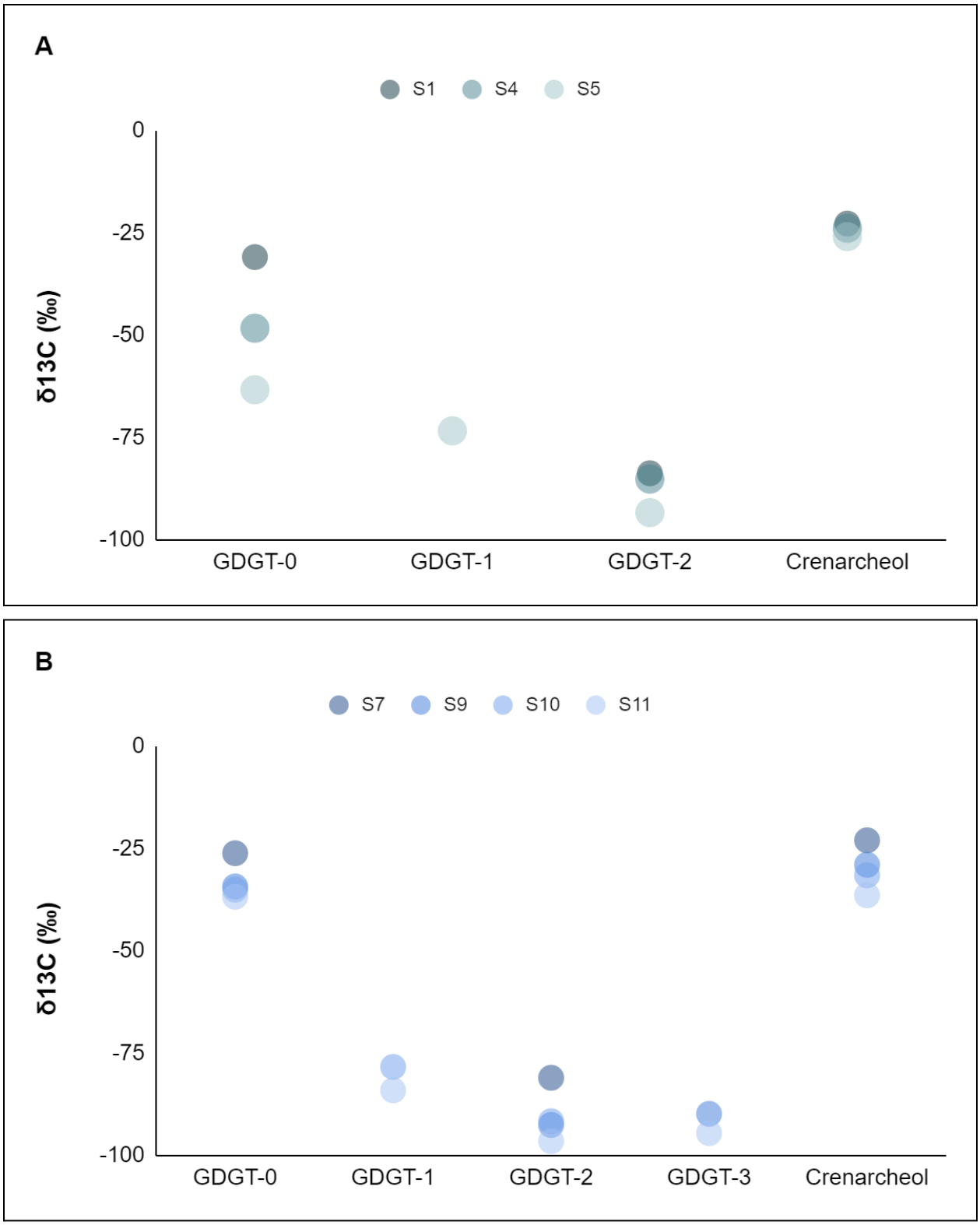

Fig. 9: $\delta^{13}C$ values for each GDGT in Core 1 (A) and Core 2 (B).

In Core 1, the variation in the $\delta^{13}C$ values seen in GDGT-0 is significantly greater than that seen in the other compounds (Fig. 9 A). There is a range of approximately 32.4‰ for GDGT-0, compared to ranges of approximately 9.61‰ and 3.19‰ for GDGT-2 and Crenarchaeol, respectively. Therefore, Crenarchaeol values do not vary widely across different core depths, while GDGT-0 values vary widely in comparison.

In Core 2, the variation in $\delta^{13}C$ for GDGTs is much smaller overall (Fig. 9 B). However, there is greater variation for GDGT-2 and Crenarchaeol in Core 2 than in Core 1. There is a range of approximately 15.45‰ for GDGT-2 and 13.43‰ for Crenarchaeol. GDGT-3 exhibits the smallest range across the different core depths, 4.71‰. For all compounds where there is a value for the coretop depth, S7 consistently exhibits the greatest difference from the average value.

In both cores, the values of $\delta^{13}C$ are the most strongly depleted in ^{13}C for GDGT-2 and are the least depleted for Crenarchaeol.

II: Relative Abundances

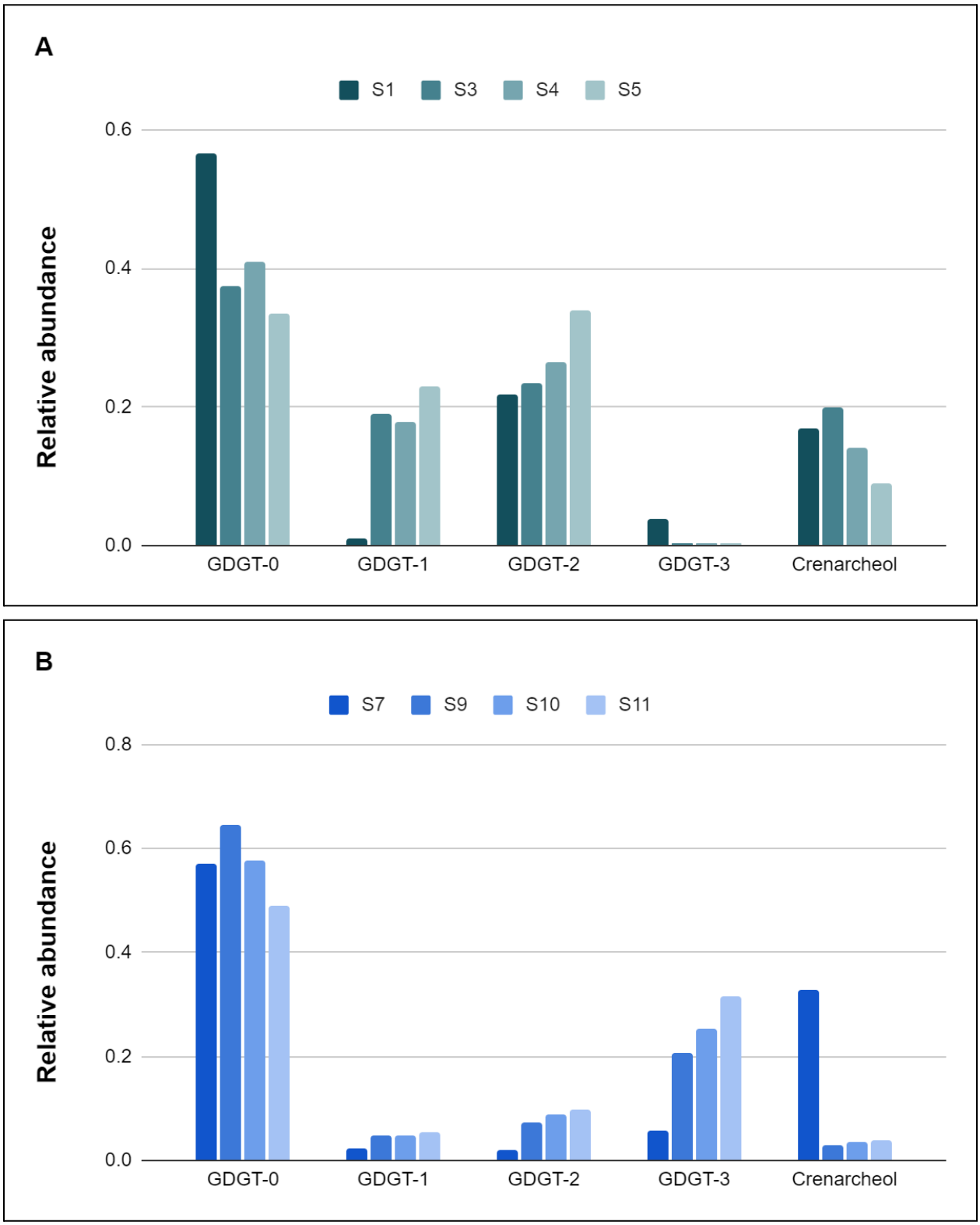

Fig. 10: Relative abundance of GDGTs in Core 1 (A) and Core 2 (B).

The sensitivity and specificity of the analyzer in QQQ-MS allows for the measurement of the area of each GDGT compound class, along with that of their isomers. Relative abundances were calculated by dividing the areas for each GDGT by the sum of the combined areas of the other GDGTs, isomers included (Fig. 10). In Core 1, GDGT-0 is the most abundant overall (average relative abundance ≈ 42.11%), followed by GDGT-2 (~26.41%), GDGT-1 (~15.21%), Crenarchaeol (~15.02%), and GDGT-3 (~1.25%) (Fig. 10 A). In Core 2, GDGT-0 is also the most abundant overall (~55.09%), followed by GDGT-3 (~20.80%), Crenarchaeol (~10.78%), GDGT-2 (~7.01%), and GDGT-1 (~4.32%) (Fig. 10 B).

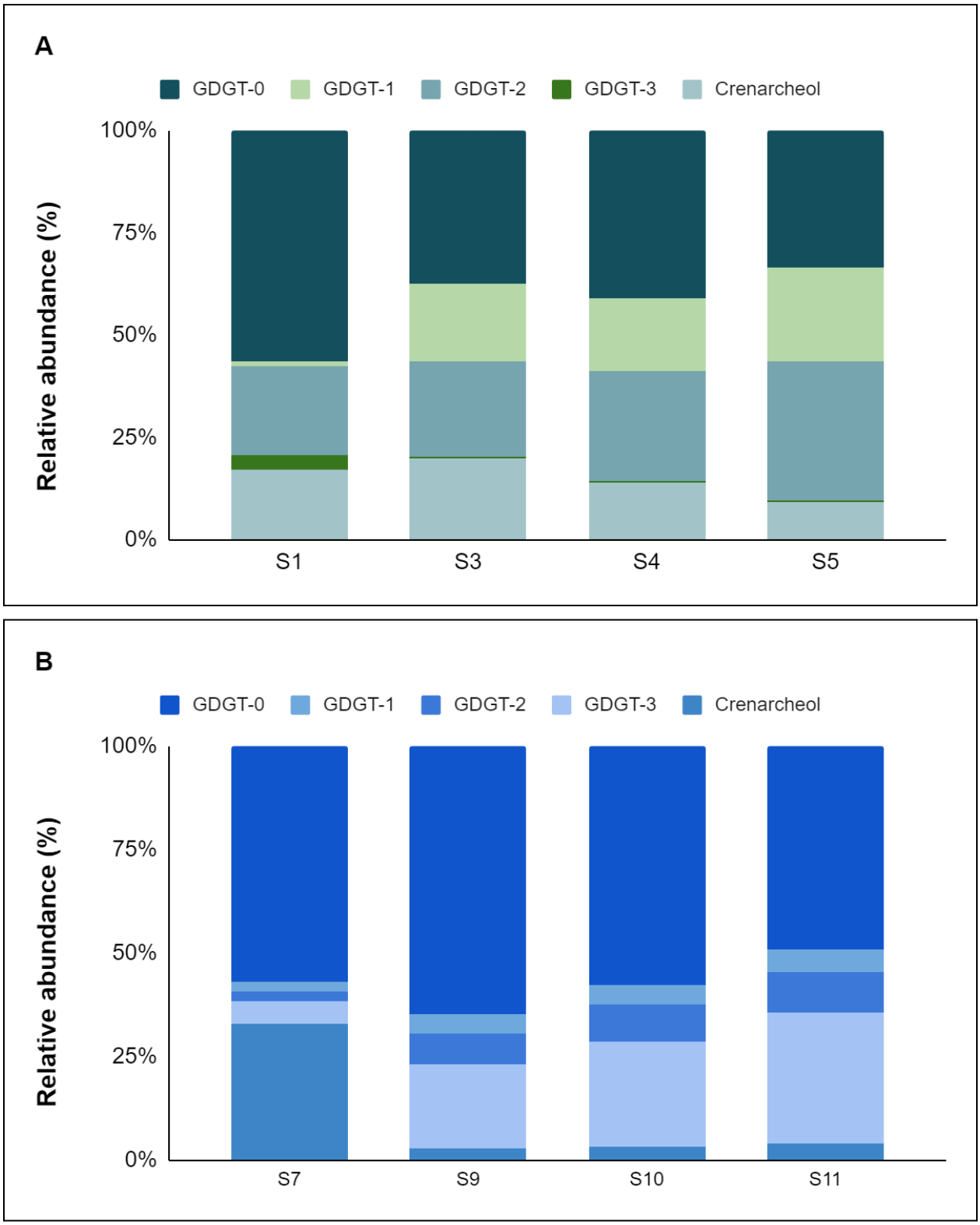

Fig. 11: Relative abundance of GDGTs in Core 1 (A) and Core 2 (B) by percentage of sample composition.

The gap between the predominant GDGT-0 and the other compounds is much larger in Core 2, 20 meters away from the seep, than in Core 1, which was taken right at the seep (Fig. 11). In Core 1, GDGT-1 and Crenarchaeol have very similar overall abundances, while Core 2 exhibits greater variation in relative abundance across compounds.

Across individual samples, S1 is an outlier in that its values for GDGT-1 and GDGT-3 are respectively much smaller and slightly larger than the average relative abundances across the whole of Core 1 (Fig. 11 A). GDGT-0 is even more predominant in S1 than in the other samples. In Core 2, S7 is an outlier in that its values for GDGT-1, GDGT-2, and GDGT-3 are respectively slightly, somewhat, and much smaller than the average values of the other samples. Crenarchaeol is much more abundant in S7 than in the other samples (Fig. 11 B).

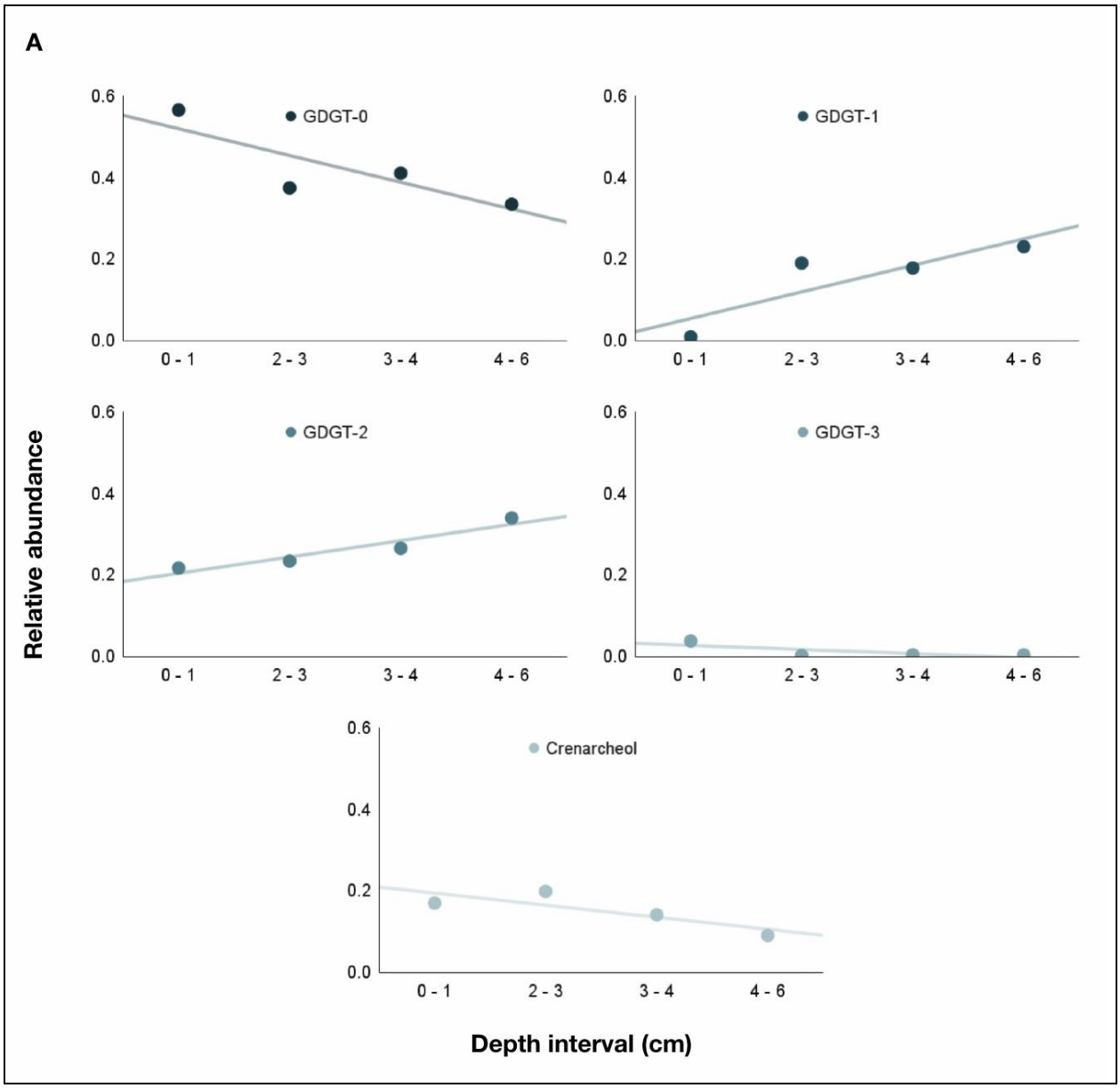

Fig. 12 A: Relative abundances of GDGTs by depth in Core 1

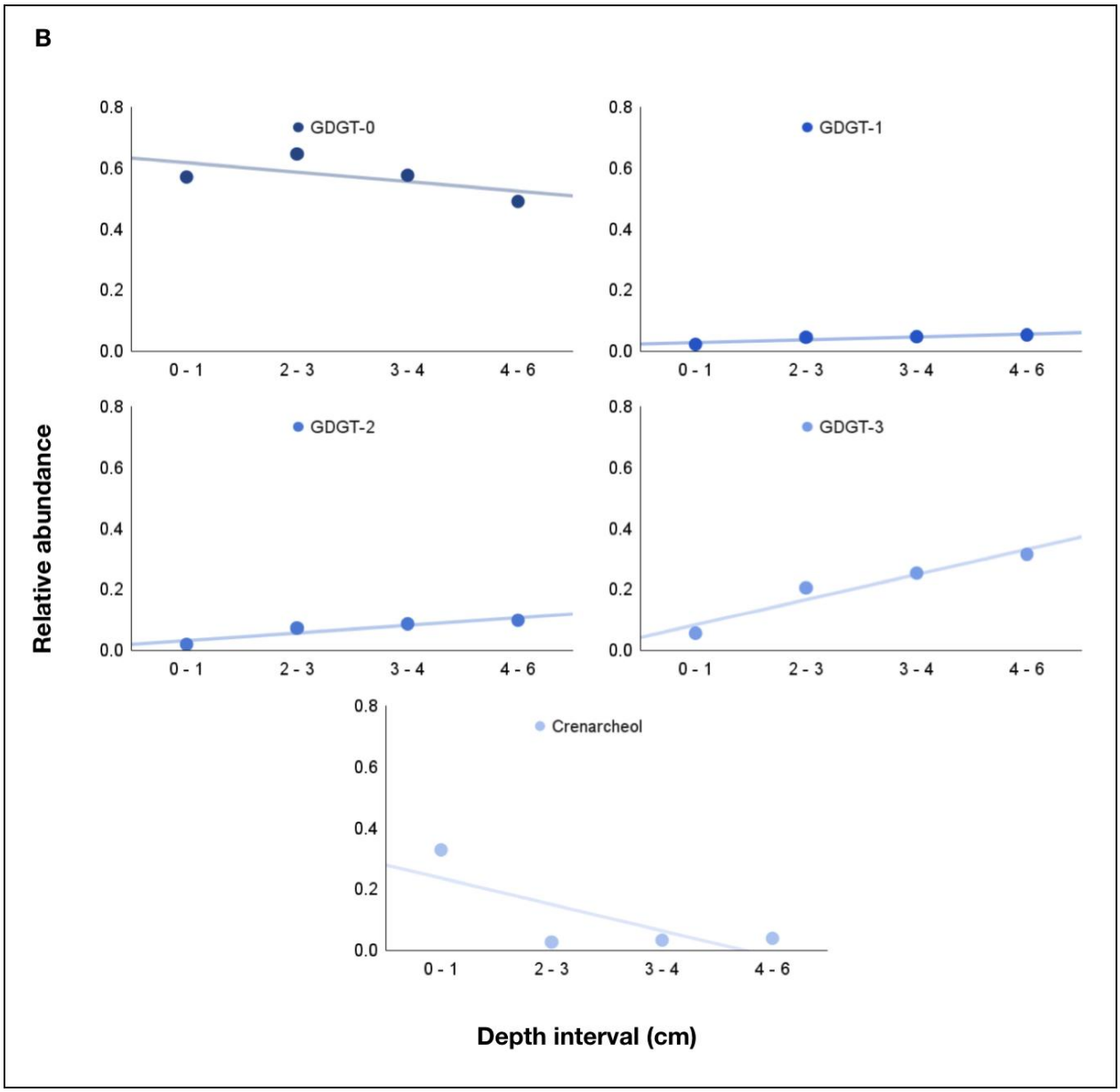

Fig. 12 B: Relative abundances of GDGTs by depth in Core 2

In Core 1, in the order of increasing intensity (i.e, slope), GDGT-3, Crenarchaeol, and GDGT-0 decrease with depth interval. Meanwhile, in the order of increasing intensity, GDGT-2 and GDGT-1 increase with depth interval (Fig. 12 A). In Core 2, (in the order of increasing intensity) GDGT-0 and Crenarchaeol decrease with depth interval (Fig. 12 B). Meanwhile, in the order of increasing intensity, GDGT-1, GDGT-2, and GDGT-3 increase with depth interval.

This is a steeper decline in relative abundance for GDGT-0 in Core 1 than seen in Core 2. GDGT-1 and GDGT-2 both increase in relative abundance more steeply in Core 1 than in Core 2, though the relative abundance of GDGT-1 rises more steeply than GDGT-2 in Core 1 and the opposite is true for Core 2. Crenarchaeol decreases more dramatically in Core 2 than in Core 1.

III: Ring Index

Ring index (RI), the average number of rings in each sample, was also derived from the areas of each GDGT compound obtained from QQQ-MS (Table 4). In this project, RI is defined as follows:

$$[\text{GDGT-0}]\times 0 + [\text{GDGT-1}]\times 1 + [\text{GDGT-2}]\times 2 + [\text{GDGT-3}]\times 3 + [\text{Cren} + \text{Cren'}]\times 4 \qquad (1)$$

Table 4: Ring indices for Core 1 and Core 2.

Depth interval (cm)	**Core 1**	**Core 2**
0 - 1	1.239	1.55
2 - 3	1.461	1.016
3 - 4	1.288	1.121
4 - 6	1.287	1.36

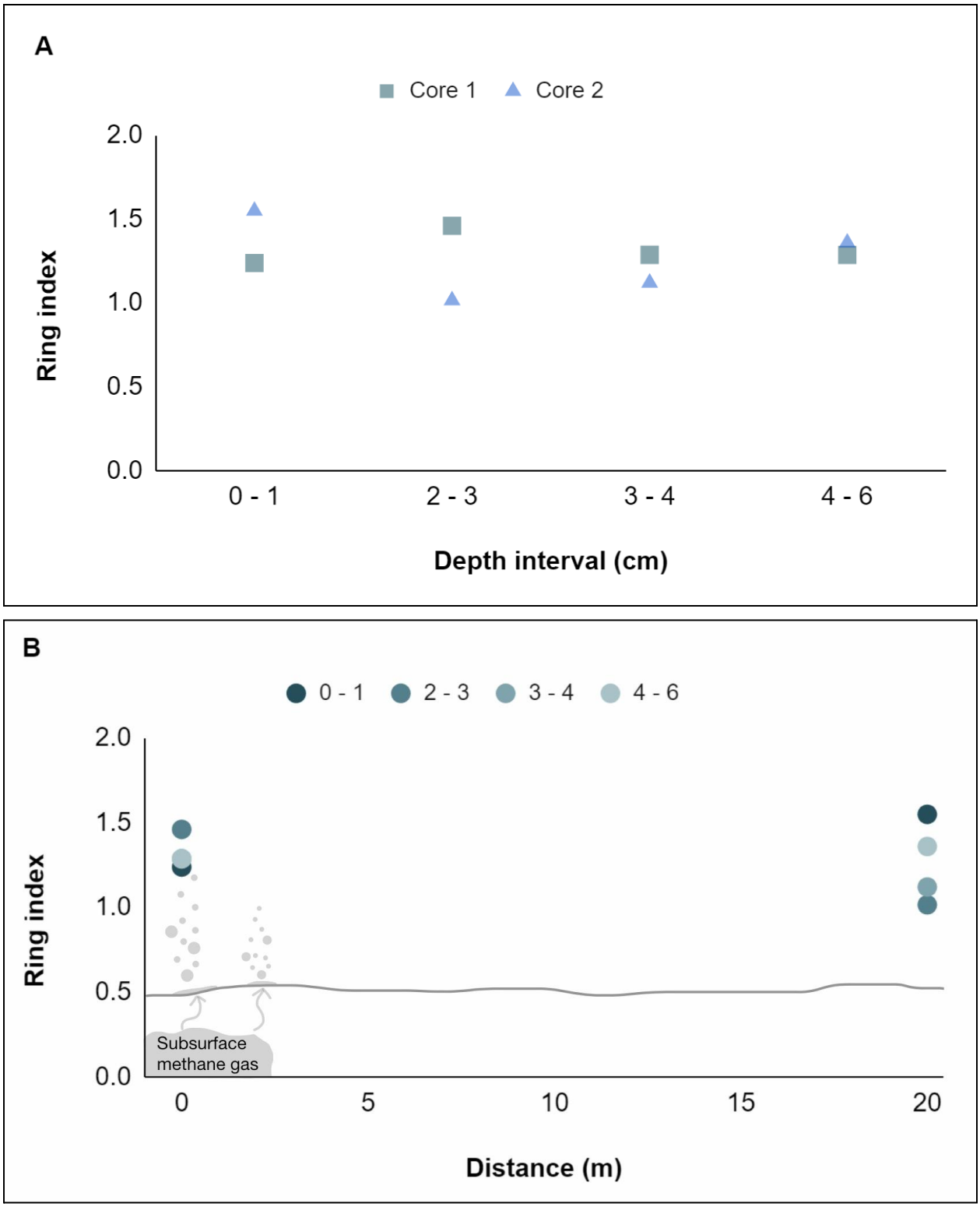

Fig. 13: Core depth interval vs. ring index (A), and distance from seep vs. ring index overlaid over a simple drawing of the site (B).

The ring indices of Core 1 and Core 2 both decrease as the depth interval increases (Fig. 13 A). Core 1 shows an extremely slight decrease, while Core 2 shows a more significant fall. This aligns with the greater range of average ring values exhibited in Core 2 than Core 1 (Fig. 13 B). However, these changes are still very minor. Perhaps more significantly, the average ring index of Core 1, 1.319, is slightly lower than that of Core 2, 1.262. Core 2 also possesses higher RI values than Core 1 in the shallowest samples and deepest samples, while Core 1 has higher RI values in the middle depth samples.

V: Chromatography

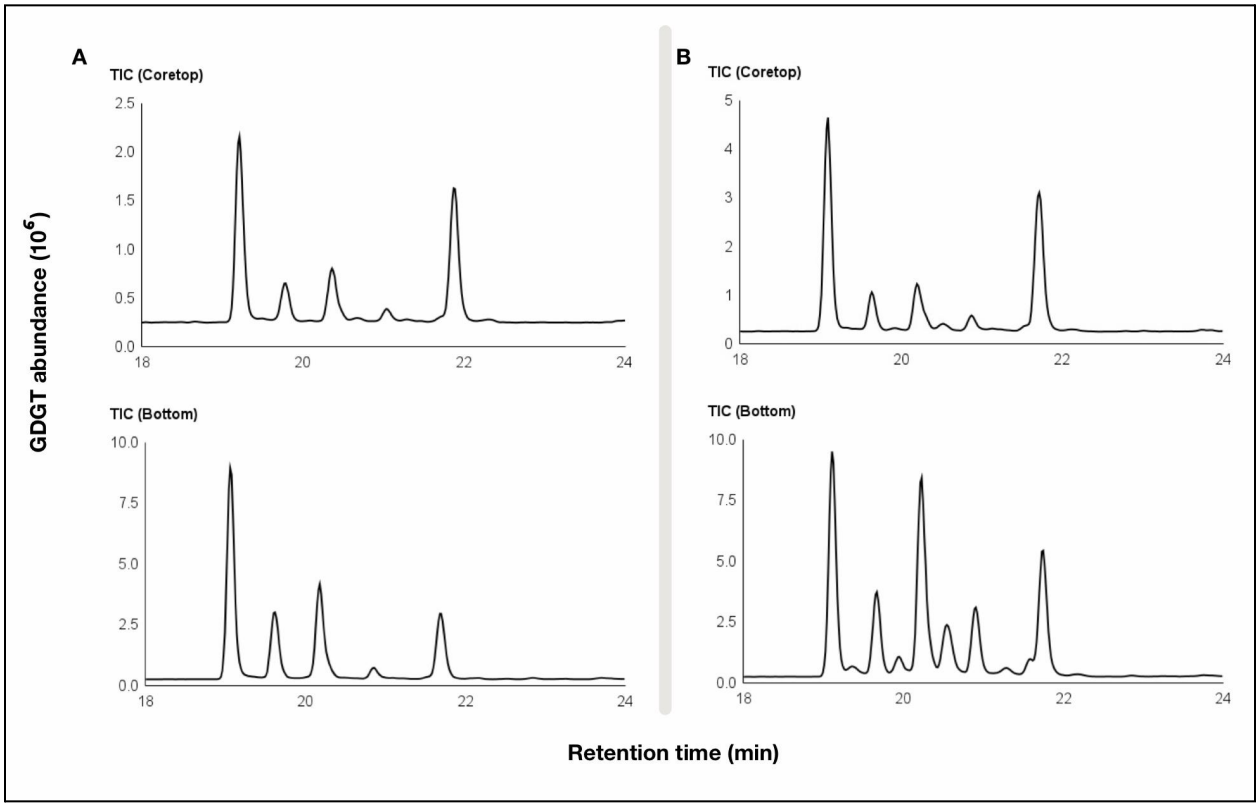

Fig. 14: Coretop and bottom TIC chromatograms for Core 1 (A) and Core 2 (B).

The coretop samples exhibit very similar chromatographic results, while the bottom sample for Core 2 exhibits far more noise than Core 1. The total ion count (TIC) of the coretop (0-1 cm) samples in Core 2 is almost twice that of Core 1 (Fig. 14). This similarity is retained across individual compounds (Fig. 15). Meanwhile, the abundance of material in the bottom (4-6 cm) samples shows more variance across cores (Fig. 14). This dissimilarity is particularly present in the GDGT-1 and GDGT-3 chromatograms (Fig. 16).

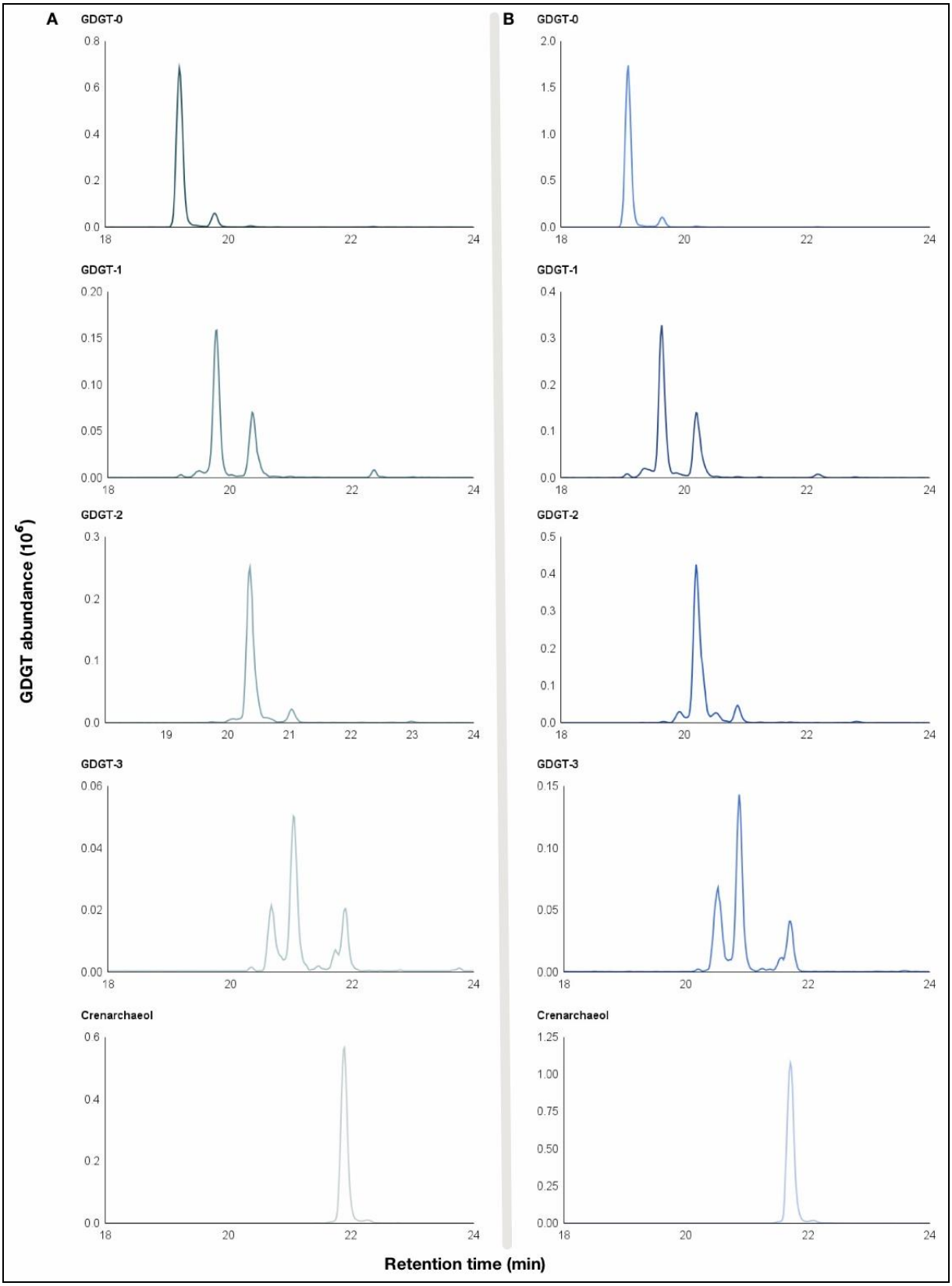

Fig. 15: Coretop chromatograms for Core 1 (A) and Core 2 (B).

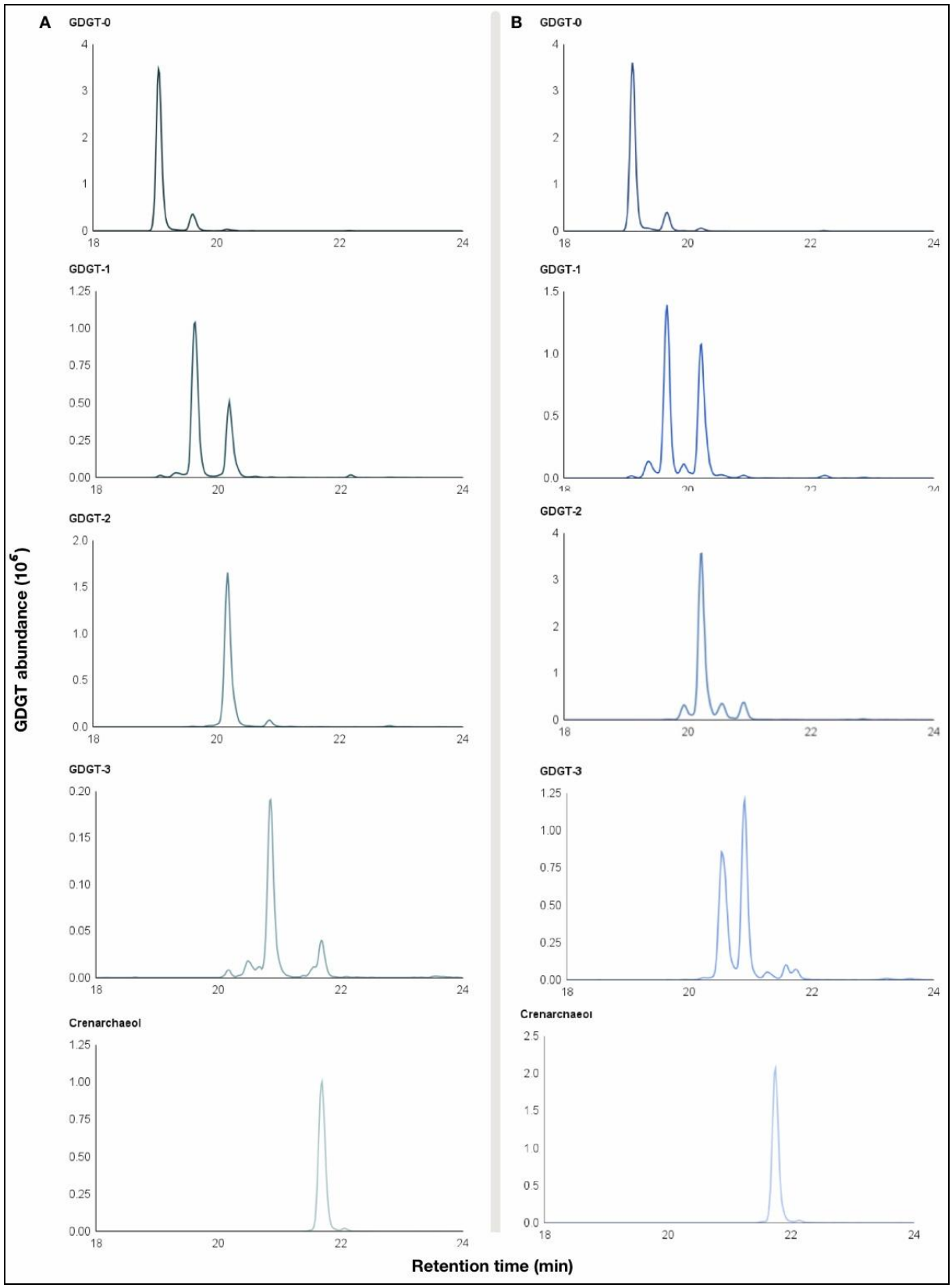

Fig. 16: Core bottom chromatograms for Core 1 (A) and Core 2 (B).

Discussion

I. Carbon Sources

Isotopic analysis of GDGTs was used to determine if these archaeal groups were predominantly taking up methane or other carbon sources.

The large variation in $\delta^{13}C$ values for GDGT-0 in Core 1 indicates greater carbon source heterogeneity, and thus greater mixing of GDGT sources, relative to GDGT-2 and Crenarchaeol in these samples. In Core 2, the variation in $\delta^{13}C$ values is smaller than in Core 1, and particularly in GDGT-0. It is therefore likely that there is less overall mixing in Core 2. However, there is greater variation for GDGT-2 and Crenarchaeol in Core 2 than in Core 1, potentially indicating greater carbon source heterogeneity for these compounds in the former core. The variation in $\delta^{13}C$ for Crenarchaeol, in particular, could also be due to impurities (e.g., other GDGTs coeluting with Crenarchaeol) influencing the carbon isotope signal.

Several assumptions were made to investigate the fractional contribution of various GDGT sources. To obtain the end members for planktonic autotrophy in the water column, a $\varepsilon_{DIC/Cren}$ value of -22 - -18‰ was assumed given that this site is similar to other pelagic ocean settings. The $\delta^{13}C$ for dissolved inorganic carbon (DIC) in the water column[13], based on the average of 100 - 1000 m water, is approximately -0.3‰ (Schmittner et al., 2013). The isotopic effect observed in GDGTs is -18.7 ± 0.4‰ (Pearson et al., 2016). In marine water column settings where carbon cycling is generally presumed to be dominated by phytoplankton production, $\delta^{13}C$ values range from -21.1 ± 0.1 to -17.9 ± 0.1‰ (Kelleyl et al., 1998; Hurley et al., 2019).

[13] A Thaumarchaeota carbon source.

The end members for heterotrophy in the water column were drawn from the $\delta^{13}C$ of dissolved organic carbon (DOC) in pore water; data was pulled from a study of sub-seafloor sediments from the Bering Sea shelf break (Ijiri et al., 2012). The end members for in-situ methanotrophy were pulled from $\delta^{13}C$ values for GDGT-2 with high purity and sufficient F2/F1 ratios. The $\delta^{13}C$ for GDGT-2 in S4, -85.14‰, was determined to be a prime candidate for a pure methane end member based on its high purity and sufficient F2/F1 ratio. The -18.7 ± 0.4‰ isotopic effect observed in GDGTs (Pearson et al., 2016) accounts nicely for the -22.14‰ gap between the $\delta^{13}C_{CH4}$ at Hydrate Ridge, -63‰ (Joseph et al., 2013), and the $\delta^{13}C_{GDGT\text{-}2}$. The end member at the other side of the range, -91.61‰, was also selected based on its high purity and sufficient F2/F1 ratio. For these values, there is high confidence that these are pure GDGTs not influenced by coelution with other factors.

The end members for in-situ heterotrophy were assumed to be the $\delta^{13}C$ of bulk total organic carbon (TOC) in the sediment; values were pulled from a study on sediments of the gas hydrate system of the northern Cascadia Margin (Kaneko et al., 2010). In the study of Bering Sea shelf break sediments, $\delta^{13}C_{TOC}$ values from samples less than 100 cm below the sediment surface were approximately -24‰ (Ijiri et al., 2012). End members are listed below (Table 5).

Table 5: End members for carbon sources[14]

Metabolism	**Source**	δ^{13}**C**	**References**
Autotrophy	Water column	$\delta^{13}C_{DIC}$ in the water column, GDGT range ≈ -22 to -18‰	Kelleyl et al., 1998; Schmittner et al., 2013; Pearson et al., 2016; Hurley et al., 2019
Heterotrophy	Water column	$\delta^{13}C_{DOC}$ in the water column ≈ -24‰ to -22‰	Ijiri et al., 2012
Methanotrophy	Sediment	$\delta^{13}C_{GDGT\text{-}2}$ at the methane seep ≈ -91.61 to -85.14‰	This study
Heterotrophy	Sediment	$\delta^{13}C_{TOC}$ in the sediment ≈ -25.7 to -21.5‰	Kaneko et al., 2010; Ijiri et al., 2012

To approximate the fractional contribution of methanotrophic sources, the focus of this project, one major assumption is made: that the only sources of GDGTs are from Thaumarchaeota or anaerobic methanotrophic (ANME) archaea. In addition, calculations were carried out under the principles that (I) the stable carbon isotope ratio of a given GDGT will equal the carbon isotope ratios of its sources given their fractional abundances (2.a); and that (II) the summed fractional abundances of the sources represent the total source (2.b). Thus,

$$\delta^{13}C_{GDGT} = \delta^{13}C_{\text{water column}} \times f_{\text{water column}} + \delta^{13}C_{\text{methanotrophy}} \times f_{\text{methanotrophy}} \quad (2.a)$$

$$1 = f_{\text{water column}} + f_{\text{methanotrophy}} \quad (2.b)$$

These equations can be manipulated to give:

[14] While only end members for heterotrophy in the water column and in-situ methanotrophy were utilized for the simple two-member fractional abundance calculations, the δ^{13}C values drawn from various papers are retained here to provide context.

$$f_{\text{water column}} = (\delta^{13}C_{GDGT} - \delta^{13}C_{\text{methanotrophy}}) \div (\delta^{13}C_{\text{water column}} - \delta^{13}C_{\text{methanotrophy}}) \quad (2.c)$$

The fractional contribution of methanotrophic sources can then be calculated using (2.c). Table 6 shows the ranges of values for fractional contributions for GDGT-0 given the values recorded in Table 5.

Table 6: Fractional contributions for GDGT-0 in Core 1 (A) and Core 2 (B).

A

Sample ID	**Depth interval (cm)**	$\delta^{13}C_{GDGT\text{-}0}$ (‰)	$f_{\text{water column}}$	$f_{\text{methanotrophy}}$
S1	0-1	-30.91	0.859 - 0.898	0.102 - 0.141
S4	3-4	-48.29	0.584 - 0.641	0.359 - 0.416
S5	4-6	-63.31	0.346 - 0.419	0.581 - 0.654

B

Sample ID	**Depth interval (cm)**	$\delta^{13}C_{GDGT\text{-}0}$ (‰)	$f_{\text{water column}}$	$f_{\text{methanotrophy}}$
S7	0-1	-26.16	0.934 - 0.968	0.032 - 0.066
S9	2-3	-34.27	0.806 - 0.848	0.152 - 0.194
S10	3-4	-35.05	0.793 - 0.837	0.163 - 0.207
S11	4-6	-36.78	0.766 - 0.811	0.189 - 0.234

In both cores, the fractional contribution of autotrophic water column sources is highest at the coretop and decreases with depth (Fig. 17). (The relative abundances calculated agree with these findings; the abundance of Crenarchaeol is highest in the coretop samples and decreases with depth as well.) In contrast, the contribution of methanotrophy for GDGT-0 is lowest in the coretop samples and increases with depth; it also rises more dramatically in Core 1 than Core 2. For Core 1, the fractional contribution of methanotrophic sources for GDGT-0 appears to overtake the fractional contribution of water column sources around 3-4 cm down into the core.

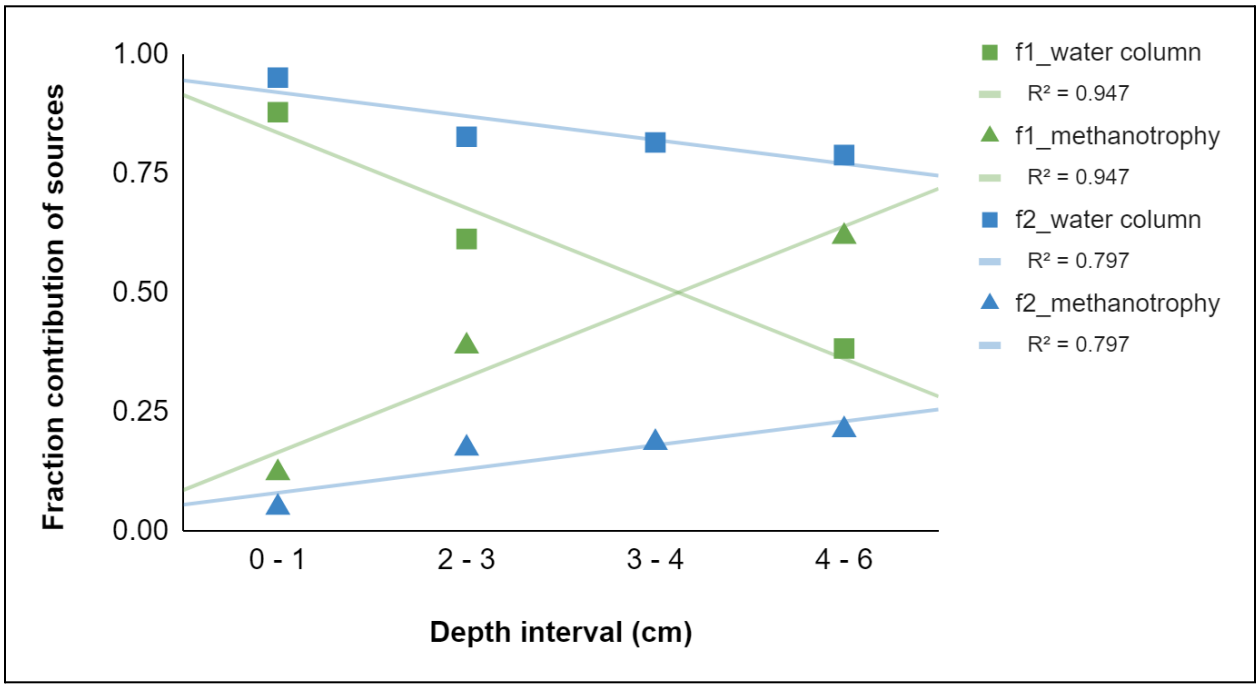

Fig. 17: Fractional contributions of methanotrophic and water column sources for GDGT-0. $f_{1,\ water\ column}$ and $f_{1,\ methanotrophy}$ refer to Core 1, while $f_{2,\ water\ column}$ and $f_{2,\ methanotrophy}$ refer to Core 2.

These findings are consistent with the expectation that the fractional contribution of carbon sourced from the water column should decrease with depth. In this setting, as the depth interval increases, it is expected that ANME populations will have an increasing impact. This impact would then be reflected in the increase of the contribution of sources besides the water column to the lipid pool—which is what is seen here.

II. Relative Abundance

Because the number of cyclopentane rings can reveal information about temperature and environmental stressors (Pearson and Ingalls, 2013), the order of ring abundances is also significant. In Core 1, GDGT-0 was the most abundant compound, followed by GDGT-2, GDGT-1, Crenarchaeol, and GDGT-3. In Core 2, GDGT-0 was followed by GDGT-3,

Crenarchaeol, GDGT-2, and GDGT-1. This might suggest greater environmental stress at the Core 2 site (right at the seep) than at the Core 1 site (20 meters away).

The relative abundances of the coretop samples, S1 (Core 1) and S7 (Core 2), are outliers. S7 is of particular interest here, given that Crenarchaeol is far more abundant than in the other Core 2 samples. The discrepancies between the coretop samples and those lower in the core are likely due to the anoxic environment of sediments deeper in the core. Thus, it is unlikely that there is any in-situ production of Crenarchaeol, a compound associated with aerobic production, deep within the cores. It is possible that there is a Thaumarchaeota community at the top of Core 2 that is producing a great deal of Crenarchaeol. Under oxic conditions, respiration releases ammonia, which could in turn feed such a community (Stahl and de la Torre, 2012; Kozlowski et al., 2016). This would also help explain why the $\delta^{13}C$ for Crenarchaeol are on the slightly lower side.

A coretop Thaumarchaeota community could also be the reason behind key trends down both cores. At both sites, the relative abundance of Crenarchaeol decreases with depth, which aligns with the above theory. At the same time, GDGT-1 and GDGT-2 increase with depth interval in both cores. This is in line with initial expectations, as these compounds are contributed by archaea that carry out AOM (anaerobic oxidation of methane), which are associated with methane hydrates (Pancost et al., 2001; Blumenberg et al., 2004; Zhang et al., 2011). Interestingly, GDGT-1 and GDGT-2 both increase in relative abundance more steeply in Core 1 than in Core 2, and Crenarchaeol decreases more dramatically in Core 2 than in Core 1.

In an attempt to investigate the factors behind these trends, I calculated the methane index (MI) for each sample. MIs are biomarker indicators used to quantify the relative contribution of methanotrophic (represented by GDGT-1, GDGT-2, and GDGT-3) vs. planktonic

(represented by Crenarchaeol and Crenarcheol-regioisomer) microbes (Zhang et al., 2011). MI is calculated using the equation below (Eq. 3).

$$MI = \frac{[GDGT\text{-}1] + [GDGT\text{-}2] + [GDGT\text{-}3]}{[GDGT\text{-}1] + [GDGT\text{-}2] + [GDGT\text{-}3] + [Cren] + [Cren']} \quad (3)$$

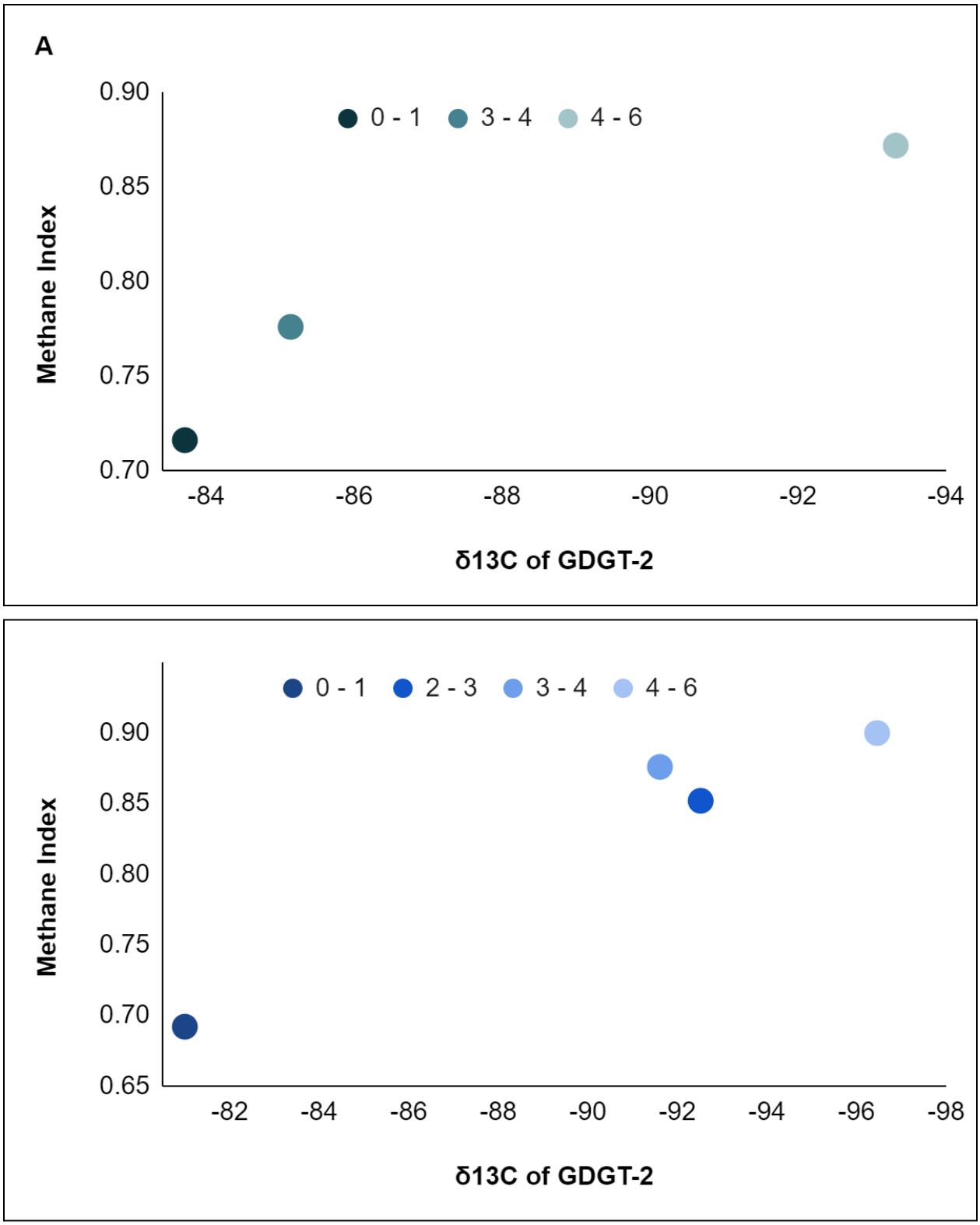

Fig. 18: Correlation between methane index and $\delta^{13}C_{GDGT\text{-}2}$ in Core 1 (A) and Core 2 (B).

High MI values reflect the substantial production of GDGT-1, GDGT-2, and GDGT-3; this suggests the significant role played by AOM microbial communities (Zhang et al., 2011). Meanwhile, low MI values—which characterize typical marine sedimentary conditions—indicate the prevalence of non-methanotrophic archaea like Thaumarcheota (Zhang et al., 2011).

In both cores, MI increases with depth interval (Fig. 18). This implies that the amount of methanotrophy also rises with depth. The rise in MI from the coretop samples to the bottom sample is slightly larger in Core 2 (0.208) than in Core 1 (0.156). This suggests that methanotrophy increases more rapidly with depth right at the seep than 20 meters away.

The average MI values of Core 1 and Core 2 are 0.788 and 0.83 respectively. These are both relatively high values, indicating the overarching predominance of AOM communities. However, the coretop values, 0.716 for Core 1 and 0.692 for Core 2, suggests that there is at least a greater community of Thaumarchaeota in the first centimeter compared to lower depths.

The lower MI values at the coretop of Core 2 compared to Core 1 is consistent with the finding that the abundance of Crenarchaeol is greater at S7 than at S1. This suggests that if there is indeed an in-situ coretop community of Thaumarchaeota at the seep, it would be larger at the actively-bubbling site than 20 meters away.

III: Ring Index

The ring indices calculated show a greater range of average RI values for Core 2 than Core 1, suggesting a greater range of environmental stress right at the seep than 20 meters away. This aligns with the relative abundance results, which appear to indicate increased stress at the Core 2 site compared with the Core 1 site.

Core 2 has higher RI values in the coretop samples and bottom samples, suggesting increased stress at the top and bottom of the core. Meanwhile Core 1 possesses higher RI values in the middle depth samples, perhaps indicating increased stress at the center of the core.

Core 2 also shows a slightly more significant decrease in RI than Core 1; it is possible that while conditions become moderately less hostile with depth at both sites, they do so somewhat more dramatically farther away from the seep. However, it is important to note that these discrepancies are very small.

IV: TEX_{86}

Another critical function of archaeal GDGTs is their role as the foundation of a sea surface temperature (SST) proxy, TEX_{86} (Schouten et al., 2002; Pearson et al., 2016), which is used for paleoclimate reconstructions over timescales ranging from the Jurassic to the modern day in large lacustrine and marine environments (Bijl et al., 2010; Tierney et al., 2010; Jenkyns et al., 2012; Pearson et al., 2016). Given the wide temporal and geographic span of these biomarkers, it is likely that GDGTs will remain a powerful tool for the interpretation of ancient temperatures over Earth history (Pearson et al., 2016). Modern TEX_{86} calculations generate strong predictions of SSTs—generally within ±3-5°C (Liu et al., 2009; Kim et al., 2010; Tierney and Tingley, 2014; Pearson et al., 2016). However, there is disagreement between ancient records of TEX_{86}-predicted SSTs and other climate models/proxies, especially during eras marked by greenhouse climates (Jenkyns et al., 2004; Hollis et al., 2012; Lopes dos Santos et al., 2013; Pearson et al., 2016). Understanding the mechanisms behind the creation, transport, and placement of GDGTs is thus crucial (Pearson and Ingalls, 2013; Pearson et al., 2016).

The areas used to calculate the TEX_{86} indices were also obtained from QQQ-MS results (Fig. 16). The calibrations for both TEX_{86}, TEX_{86}^{L}, and TEX_{86}^{H} all omit GDGT-0, as this compound can have multiple sources (Koga et al., 1993). Because Crenarchaeol is often more abundant than its isomer and other GDGT compounds by an order of magnitude, and does not exhibit any correlation with SST, it is excluded as well (Kim et al., 2010).

Based on a global sediment study of 44 coretops (Schouten et al., 2002), TEX_{86} was originally defined as:

$$TEX_{86} = \frac{[GDGT\text{-}2]+[GDGT\text{-}3]+[Cren']}{[GDGT\text{-}1]+[GDGT\text{-}2]+[GDGT\text{-}3]+[Cren']} \quad (4.a)$$

Based on a global dataset of 284 coretops (Kim et al., 2008), TEX_{86} is correlated to SST using the following calibration equation below, for which there is an error of ±1.7 °C.

$$TEX_{86}^{O}\text{-}SST = 56.2 \times TEX_{86} - 10.8 \quad (4.b)$$

The TEX_{86}^{L} index was later proposed based on an extensive study of 396 coretops, in which the correlation of all the possible combinations of GDGTs was compared with SST (Kim et al., 2010). The index excludes Crenarchaeol-regioisomer and removes GDGT-3 from the numerator. There is a calibration error of ±4 °C (Kim et al., 2010).

$$TEX_{86}^{L} = \log_{10}\frac{[GDGT\text{-}2]}{[GDGT\text{-}1]+[GDGT\text{-}2]+[GDGT\text{-}3]} \quad (5.a)$$

TEX_{86}^{L} is correlated to SST using the following calibration equation:

$$TEX_{86}^{L}\text{-}SST = 67.5 \times TEX_{86}^{L} + 46.9 \quad (5.b)$$

The TEX_{86}^{H} index, proposed alongside the TEX_{86}^{L} index, is based on the examination of 255 coretops and has a calibration error of ±2.5 °C (Kim et al., 2010). TEX_{86}^{H} is correlated to SST using the following calibration equation:

$$TEX_{86}^{H}\text{-SST} = 68.4 \times \log_{10}TEX_{86} + 38.6 \quad (6)$$

As to be expected, the temperatures derived from TEX_{86} and TEX_{86}^{H} agree highly with each other. The trendline of temperatures calculated from TEX_{86}^{L} is almost exactly parallel to that of TEX_{86}, but the values are shifted up by approximately 10 °C (see Appendix, Fig. 23).

One goal was to compare these TEX_{86} values with real SST data. The temperature-dependence of GDGT distributions has been largely described as a physiological property of planktonic Thaumarchaeota[15] (Schouten et al., 2002; Zhang et al., 2011). If the GDGTs were purely sourced from the water column, the TEX_{86}-calculated temperatures would have generated an accurate signal.

This comparison was carried out under the assumption that each sample layer corresponds to a period of time for which there was relatively stable sea surface temperature. Once the rate of sedimentation was determined, SSTs corresponding to the time period in which the sediment was deposited could be compared with TEX_{86}-calculated values. The average sediment accumulation rate at Astoria Canyon is approximately 260 mg/cm^2/year (Carpenter et al., 1982). The average dry weight of sediment per centimeter of sample is ~0.726 g/cm^3.[16] Thus, the average depositional rate of sedimentation at Astoria Canyon is ~0.358 cm/year. Each centimeter down a core therefore represents ~2.793 years. SSTs were drawn from the Coastal Data Information Program database[17].

---

[15] The Zhang et al., 2011 and Schouten et al., 2002 papers specifically mention Crenarchaeota, which was thought to include Thaumarchaeota (initially classified as mesophilic Crenarchaeota) until after the manuscript was published. Comparative genomics later revealed that Thaumarchaeota is in fact a distinct and "deep-branching" archaeal phylum (Pester et al., 2011).

[16] The average dry weight of sediment per centimeter of sample is ~32.0698 g, and the volume of each sample core slice is ~44.1787 cm^3.

[17] http://cdip.ucsd.edu/m/products/?stn=179p1; http://cdip.ucsd.edu/themes/?zoom=auto&tz=UTC&ll_fmt=dm&numcolorbands=10&palette=cdip_classic&high=6.096&r=999&un=1&pb=1&d2=p70&u2=s:179:st:1:v:min_max_mean:dt:202203

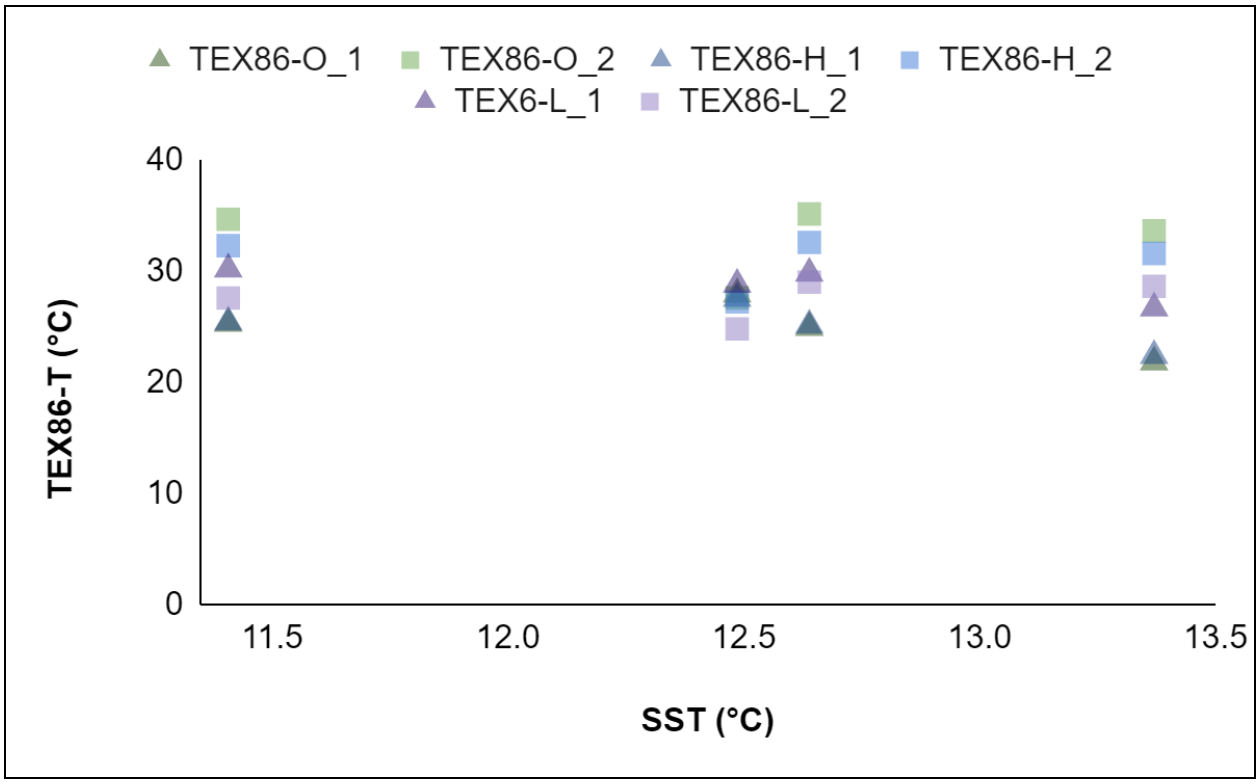

Fig. 19: TEX_{86}-calculated SSTs. TEX_{86}^{O}-calculated temperatures are green, TEX_{86}^{H}-calculated temperatures are blue, and TEX_{86}^{L}-calculated temperatures are purple. Triangles indicate values calculated from Core 1 data; squares indicate values calculated from Core 2 data.

Temperatures calculated with the TEX_{86}^{O} index were within ±15.488 °C and ±23.309 °C of the mean SSTs for the appropriate ~2.793-year (~1019-day) time period, for Core 1 and Core 2 respectively (Fig. 19). Temperatures calculated with the TEX_{86}^{H} were within ±15.091 °C and ±20.933 °C of the mean SSTs, for Core 1 and Core 2 respectively. Temperatures derived using the TEX_{86}^{L} index were within ±18.808 °C and ±16.414 °C of the mean SSTs, for Core 1 and Core 2 respectively.

The temperatures generated from the coretop sample data were generally slight outliers. In Core 1 they were 2.430 - 2.954 °C greater than the average (the exception being the temperatures from TEX_{86}^{L}). In Core 2, the coretop-derived temperatures were 2.714 - 5.174 °C

lower than the average. The same general observation applies to the errors calculated for the temperatures.

Based on the comparison of SSTs obtained from both indices, it is recommended that TEX_{86}^{H} should be applied above 15 °C and TEX_{86}^{L} below 15 °C (Kim et al., 2010). All the SSTs from Astoria Canyon were under 15 °C, so it was expected that TEX_{86}^{L} would generate more accurate temperatures. However, interestingly enough, there was slightly more error in the TEX_{86}^{L}-derived temperatures than in the TEX_{86}^{H}-derived temperatures.

Overall, the TEX_{86} temperatures greatly overestimated the SSTs. Even the smallest underestimations, from the TEX_{86}^{O} temperatures for Core 1, underestimated SSTs by at least 8.459 °C. Values generated by all three indices fall significantly outside the range of acceptable error.

Valuable information was gleaned from the TEX_{86} data. The high amount of error indicates that sources besides the water column contributed to the GDGTs, as expected. If the TEX_{86}-calculated temperatures had instead produced a reliable temperature proxy, the GDGTs would have had to be purely sourced from the water column, which could directly contradict much of the data collected here.

The high amount of error may also indicate the inaccuracy of estimated sediment accumulation rate for the sample location. Additionally, previous work by the Pearson Lab shows that exogenous sources have a significant influence on GDGTs in a great deal of slope/shelf sediments (Pearson et al., 2016). The Cascadia region lies on a long, sloping subduction zone with many active tectonic processes due to the underthrusting of North America by the Juan de Fuca, Explorer, and Gorda plates (Spence, 1989). The significant error here may suggest the greater-than-average influence of such exogenous sources, which potentially insert

both environmental and temporal complications (Pearson et al., 2016). Differentiating between terrigenous and genuinely marine sources becomes difficult, as does determining the time periods associated with such sediments (Pearson et al., 2016). Interestingly, the error is especially high in the coretop samples, where the aforementioned possible Thaumarchaeota community would exist.

Determining the level of impact of these exogenous sources could be used to great effect in informing further assessment of the influence of the ANME populations.

V: Chromatography

As anticipated, the TIC chromatograms match the established pattern typical of a cold marine environment (Fig. 20). Though there is moderate noise in the Astoria Canyon samples studied here (particularly in the bottom sample of Core 2), the results align well with established chromatography representative of similar settings (Wuchter et al., 2004; Schouten et al., 2000 and 2002; Zhang et al., 2011).

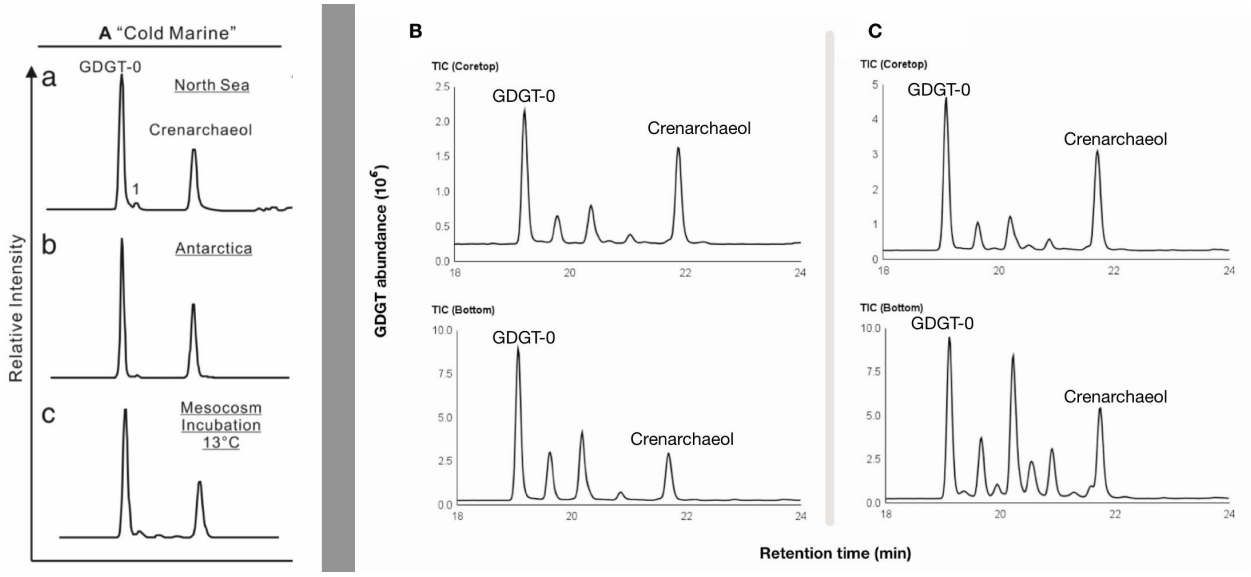

Fig. 20: Cold marine chromatography vs TIC chromatograms. Chromatograms showing the GDGT distribution in a "cold (normal) marine" environment (Zhang et al., 2011) (A) - Skagerrak, North Sea (Schouten et al., 2000) (a); Halley Bay, Antarctica (Schouten et al., 2002) (b); mesocosm incubation at 13 °C for 3 months (Wuchter et al., 2004) (c). Chromatography showing the GDGT distribution of coretop and bottom samples in Core 1 (B) and Core 2 (C).

These results are also consistent with the relative abundances calculated; the pattern of which (Fig. 10) roughly matches that exhibited in the TIC chromatography (Fig. 14). In particular, the predominance of GDGT-0 is illustrated very clearly in both of the relative abundance charts, in line with the chromatography results.

To explore differences in GDGT distributions in complex systems, the chromatograms from the cold methane seep studied here were compared with those representing other sites. At normal warm marine seeps, the relative abundance of GDGT-0 is much lower compared to in cold methane seeps. Instead, Crenarchaeol dominates, attaining peaks in relative intensity comparable to those of GDGT-0 in cold methane seeps. The peaks of GDGT-1, GDGT-2, GDGT-3, and Crenarchaeol-regioisomer are more pronounced at warmer marine environments as well; they possess higher relative abundances at such sites (Liu et al., 2009; Schouten et al., 2002; Wuchter et al., 2004; Zhang et al., 2011).

At gas hydrate impact (i.e., methane-impacted) environments, GDGT-1 and GDGT-2 possess the highest relative abundances, though they do not dominate as GDGT-0 and Crenarchaeol do at, respectively, cold and warm marine environments. GDGT-0, GDGT-1, and GDGT-2 have very prominent peaks, with the differences in relative intensity between these compounds varying widely (though the latter two are consistently the most abundant). GDGT-3 exhibits a smaller but significant peak at some sites, and Crenarchaeol has identifiable peaks but remains the less abundant compound (Pancost et al., 2001; Wakeham et al., 2003 and 2004; Stadnitskaia et al., 2008; Zhang et al., 2011).

These differences are exhibited in Fig. 21, adapted from Zhang et al., 2011, which depicts the GDGT distributions of warm marine and methane-impacted environments.

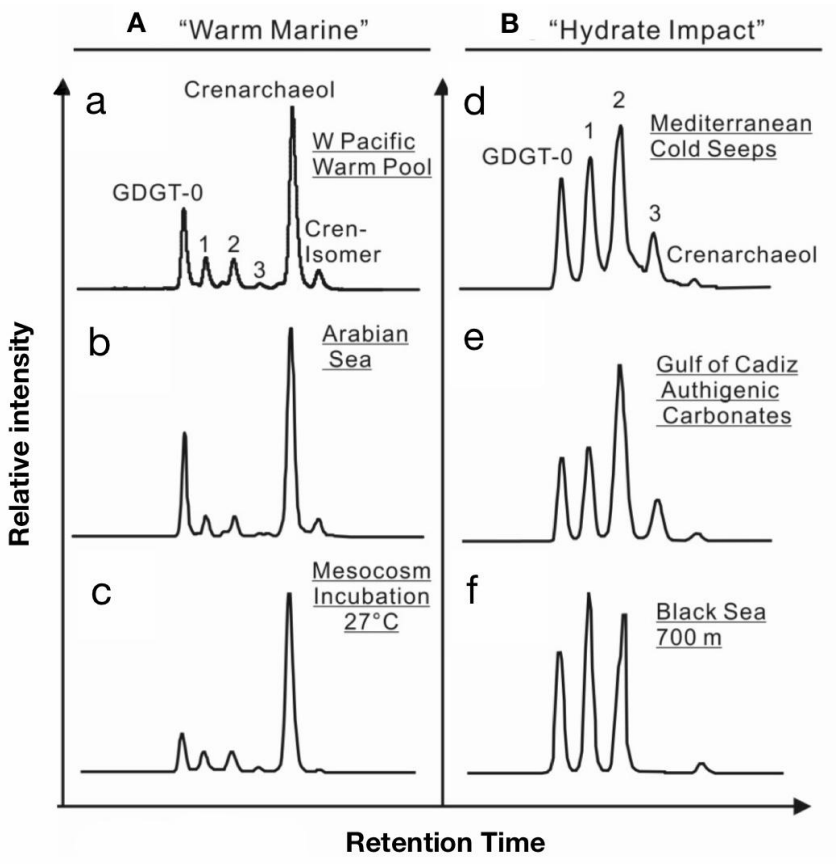

Fig. 21: Chromatograms showing the GDGT distribution in a "warm (normal) marine" environment (Zhang et al., 2011) (A) - Holocene sediments from ODP 806 at the center of the Western Pacific Warm Pool (Liu et al., 2009) (a); surface sediments from the Arabian Sea (Schouten et al., 2009) (b); mesocosm incubation at 13 °C for 3 months (Wuchter et al., 2004) (c). Chromatograms showing the GDGT distribution in a "methane impacted" environment (Zhang et al., 2011) (B) - Mediterranean cold seeps (Pancost et al., 2001) (d); Gulf of Cadiz authigenic carbonates (Stadnitskaia et al., 2008) (e); Black Sea water depth at 700 m (Wakeham et al., 2003 and 2004) (f).

VI: Future Work

Genetic information about these archaea would elevate the geochemical data collected here. The identity of the archaea could be determined via optimized DNA extraction methods that target hypervariable regions unique to this taxonomic domain.

The Girguis Lab is in possession of raw metagenomics data that, refined, would allow for an examination of whole genomes. In addition to determining the microbial composition of the

samples with high confidence, it would be possible to search for metabolic capacity by looking for specific genes, such as those associated with methanotrophy.

In addition to 16s rRNA sequencing analysis, further data could be integrated from the Girguis group and their collaborators concerning the methane and sulfate concentrations of the environment from which the samples were collected. Sulfate levels could be used to determine whether some ANME (specifically ANME-1) archaea could oxidize methane by themselves. ANME, which have never been successfully grown in pure culture, cannot carry out their metabolism when they are oxidizing methane on their own; they can only function through a chemosymbiotic relationship involving sulfate-reducing archaea (which couple methane oxidation to sulfate reduction) (Omoregie et al., 2009).

This data, which could not be gathered due to time constraints, could be used to further interpret the lipid results derived in the Pearson Lab. For example, whether the carbon isotope ratios of GDGTs sampled from different sediment depths change in tandem with environmental methane concentrations could be investigated by comparing $\delta^{13}C_{GDGTs}$ with respect to the methane levels measured at those same sites.

A return trip would allow for investigation of the existence of the suggested coretop Thaumarchaeota community. Such an outing could also include the direct measurement of the sedimentation rate directly at the site, which could then be used to confirm or recalculate the relationship between the TEX_{86}-calculated temperature and the SSTs. Additionally, further cores from smaller increments of distance from the bubble plume at the methane seep would generate more precise data.

Finally, in addition to the two push cores from Astoria Canyon examined in this project, there are similarly-prepared samples from ten cores from Nehalem Bank, Hydrate Ridge,

McArthur Promontory. Gathering data from these diverse locations would allow for the identification of key similarities and differences between cold methane seeps, no doubt yielding fascinating insights.

Conclusion

Knowledge of the environmental conditions that can give rise to and maintain life on Earth is the best basis available for identifying potential extraterrestrial habitats. The goal of this project was to study marine archaeal communities at a cold methane seep in Astoria Canyon by analyzing the carbon isotopic composition of their GDGTs, along with their abundances.

The major objectives of this project were to (I) determine if these archaeal groups are predominantly taking up carbon from autotrophic sources in the water column or from in-situ methanotrophic sedimentary sources; (II) quantify the actual contribution of archaeal methanotrophic metabolism; and (III) explore how GDGT distributions in complex systems like a cold methane seep differ from other sites.

(I, II) Overall, the archaeal groups appear to be taking up more carbon from autotrophic water column sources than from methanotrophic sources. However, the fractional contribution of the former is highest at the coretop and decreases with depth both at the seep and 20 meters away. This is consistent with the expectation that the fractional contribution of autotrophically-sourced carbon from the water column should decrease with depth as the influence of ANME populations rises. In Core 1 in particular, at the deepest depth interval, the fractional contribution of methanotrophic sources exceeds that of autotrophic sources.

The relative abundances calculated support these findings; the abundance of Crenarchaeol is highest in the coretop samples and decreases with depth as well. The chromatography results are also in agreement; the abundance of Crenarchaeol decreases relative to the amount of GDGT-0 in both cores.

In much of the data collected the uppermost samples are significant outliers, an observation that may be explained by a possible active Thaumarchaeota community in the

coretop; further examination is required to confirm the existence and ascertain the impact of such a community.

(III) The chromatography showing the GDGT distribution in the Astoria Canyon cold methane seep is consistent with the chromatography of a typical cold marine environment. In contrast, at normal warm marine seeps, the relative abundance of Crenarchaeol is much higher and the abundance of GDGT-0 is much lower. At methane-impacted environments, GDGT-1 and GDGT-2 consistently possess the highest relative abundances, though the compound with the highest relative intensity varies and GDGT-0 also has prominent peaks.

Despite the harsh conditions, microbial life thrives at this and other cold methane seeps. Given this remarkable abundance, it is well within the realm of possibility that similarly extremophilic life could evolve and flourish in analogous extraterrestrial environments. Such organisms might occupy the same niches as the archaea studied here, possibly sustained by the same carbon sources. Developing a strong understanding of the signals—whether carbon isotope ratios, relative compound abundances, or chromatographic patterns—that typify terrestrial analogue sites, and the differences between signals drawn from different sites, can provide a foundation for interpreting similar signals on other worlds.

Ultimately, this project presents several insights into an intriguing microbial ecosystem, and offers a number of avenues for further exploration.

Appendix

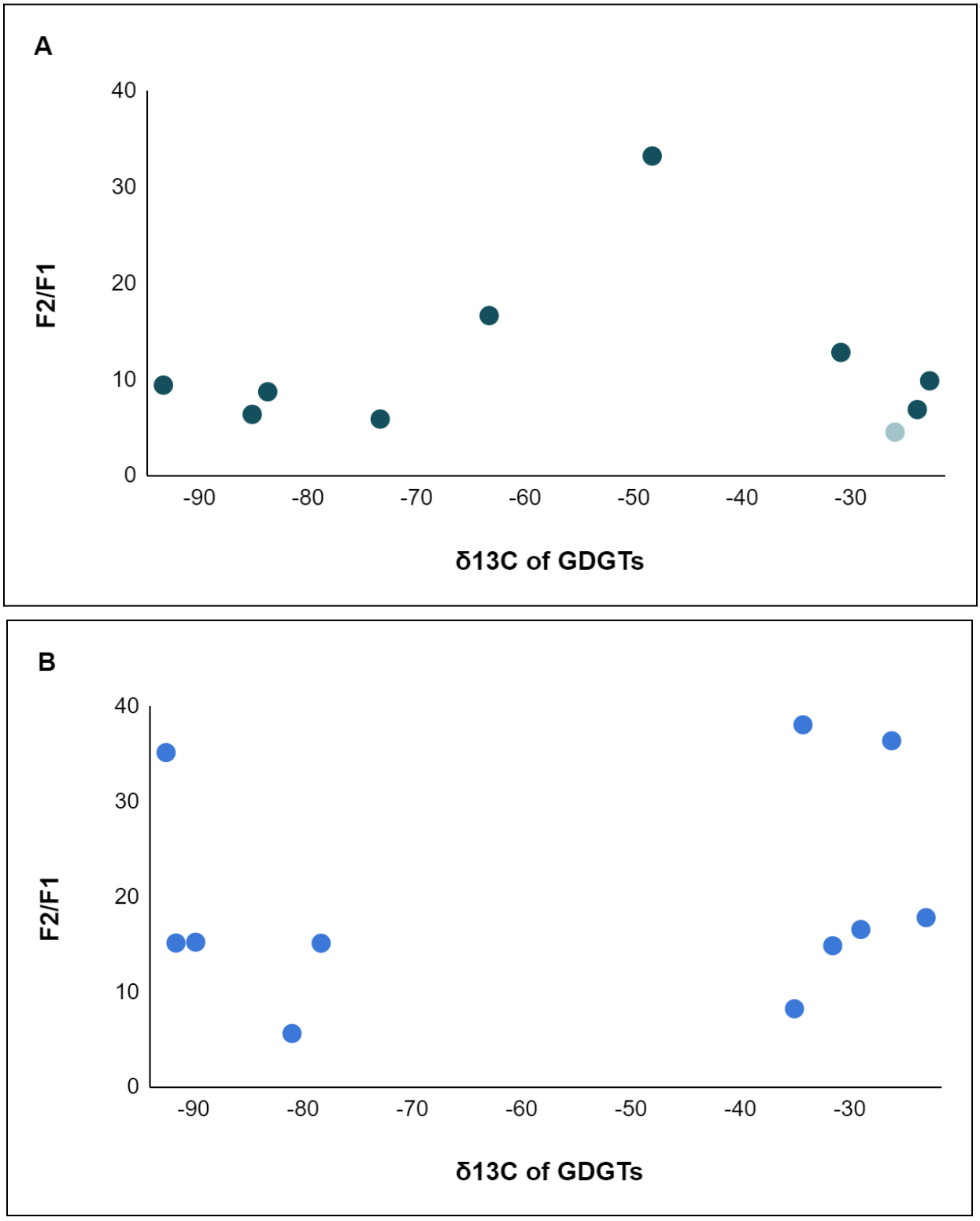

Fig. 22: F2/F1 vs $\delta^{13}C_{GDGT}$ for Core 1 (A) and Core 2 (B). Low F2/F1 (≤5) values are indicated with 50% opacity (i.e., a lighter color).

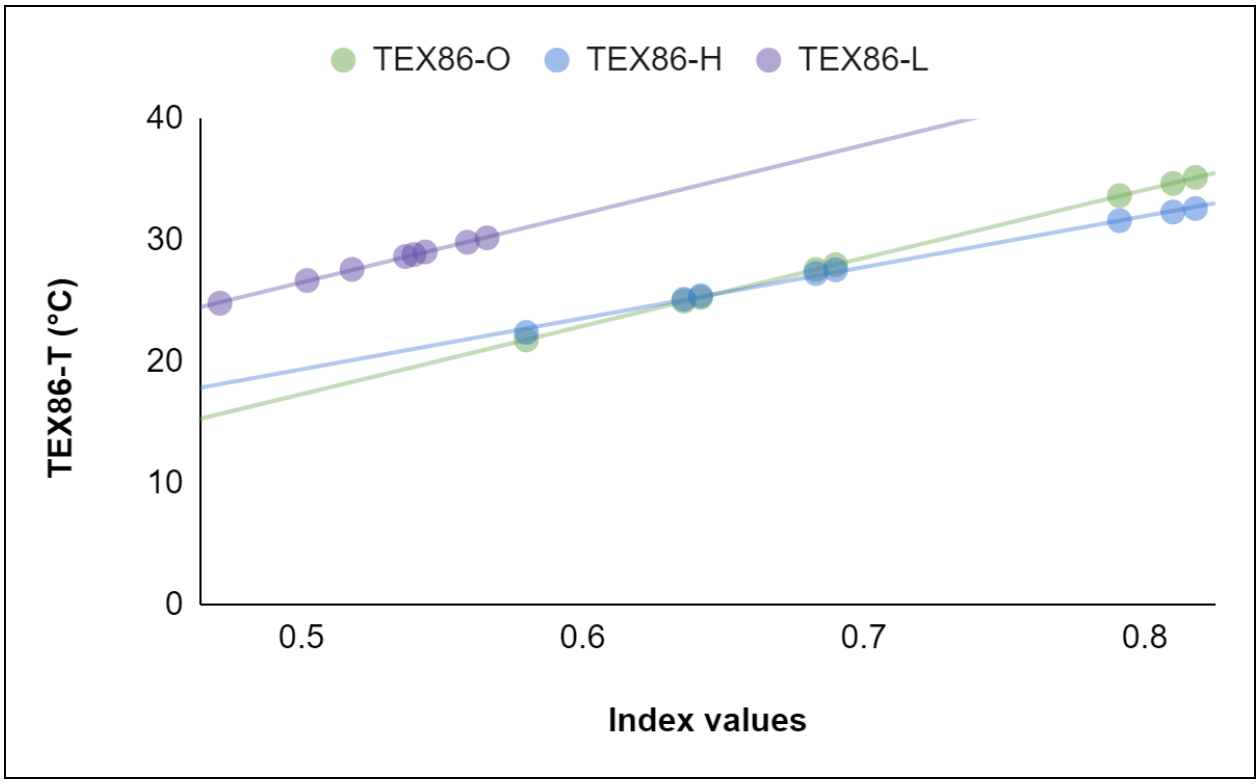

Fig. 23: Index values vs. TEX_{86}^{O}-, TEX_{86}^{H}-, and TEX_{86}^{L}-calculated temperatures.

References

1. Allers, T. & Mevarech, M. (2005). Archaeal genetics — the third way. *Nature Rev. Gen.* 6, 58–73. doi: 10.1038/nrg1504.
2. Besseling, M. A., Hopmans, E. C., Bale, N. J., Schouten, S., Damsté, J. S. S., & Villanueva, L. (2020). The absence of intact polar lipid-derived GDGTs in marine waters dominated by Marine Group II: Implications for lipid biosynthesis in Archaea. Scientific Reports, 10(1). https://doi.org/10.1038/s41598-019-57035-0.
3. Bijl, P. K., Houben, A. J. P., Schouten, S., Bohaty, S. M., Sluijs, A., Reichart, G. J., Sinninghe Damsté, J. S., & Brinkhuis, H. (2010). Transient Middle Eocene Atmospheric CO 2 and Temperature Variations. *Science*, *330*(6005), 819–821. https://doi.org/10.1126/science.1193654,
4. Blake RE, Alt JC, Martini AM. Oxygen isotope ratios of PO4: an inorganic indicator of enzymatic activity and P metabolism and a new biomarker in the search for life. *Proc Natl Acad Sci* USA. 2001 Feb 27;98(5):2148-53. doi: 10.1073/pnas.051515898. PMID: 11226207; PMCID: PMC30107.
5. Blumenberg, M., Seifert, R., Reitner, J., Pape, T., & Michaelis, W. (2004). Membrane lipid patterns typify distinct anaerobic methanotrophic consortia. *Proceedings of the National Academy of Sciences*, *101*(30), 11111–11116. https://doi.org/10.1073/pnas.0401188101.
6. Boyd, E. S., Pearson, A., Pi, Y., Li, W. J., Zhang, Y. G., He, L., Zhang, C. L., & Geesey, G. G. (2011). Temperature and pH controls on glycerol dibiphytanyl glycerol tetraether lipid composition in the hyperthermophilic crenarchaeon Acidilobus sulfurireducens. *Extremophiles*, *15*(1), 59–65. https://doi.org/10.1007/s00792-010-0339-y.
7. Buan, N. R. (2018). Methanogens: pushing the boundaries of biology. Emerging Topics in Life Sciences, 2(4), 629–646. https://doi.org/10.1042/etls20180031.
8. Carpenter, R., Peterson, M., & Bennett, J. (1982b). 210Pb-derived sediment accumulation and mixing rates for the Washington continental slope. *Marine Geology*, *48*(1–2), 135–164. https://doi.org/10.1016/0025-3227(82)90133-5.
9. Cavicchioli R. Extremophiles and the search for extraterrestrial life. (2020). *Astrobiology.* 2(3):281-92. doi: 10.1089/153110702762027862.
10. Chaban, B., Ng, S. Y. M. & Jarrell, K. F. (2006). Archaeal habitats — from the extreme to the ordinary. *Can. J. Microbiol.* 52, 73–116. doi: 10.1139/w05-147. PMID: 16541146.
11. DeLong, E. F. (1992). Archaea in coastal marine environments. *Proc. Natl Acad. Sci.* USA 89, 5685–5689. doi: 10.1073/pnas.89.12.5685.
12. De Rosa, M., Gambacorta, A., & Gliozzi, A. (1986). Structure, biosynthesis, and physicochemical properties of archaebacterial lipids. *Microbiological reviews*, *50*(1), 70–80. https://doi.org/10.1128/mr.50.1.70-80.1986.
13. Ding, ZW., Lu, YZ., Fu, L. *et al.* Simultaneous enrichment of denitrifying anaerobic methane-oxidizing microorganisms and anammox bacteria in a hollow-fiber membrane

biofilm reactor. *Appl Microbiol Biotechnol* 101, 437–446 (2017). https://doi.org/10.1007/s00253-016-7908-7.

14. Elling, F.J., Gottschalk, J., Doeana, K.D. *et al.* Archaeal lipid biomarker constraints on the Paleocene-Eocene carbon isotope excursion. *Nat Commun* 10, 4519 (2019). https://doi.org/10.1038/s41467-019-12553-3.
15. Elvert, M., Suess, E., Greinert, J., & Whiticar, M. J. (2000). Archaea mediating anaerobic methane oxidation in deep-sea sediments at cold seeps of the eastern Aleutian subduction zone. *Organic Geochemistry*, *31*(11), 1175–1187. https://doi.org/10.1016/s0146-6380(00)00111-x.
16. Foucher, J. P., Westbrook, G., Boetius, A., Ceramicola, S., Dupré, S., Mascle, J., Mienert, J., Pfannkuche, O., Pierre, C., & Praeg, D. (2009). Structure and Drivers of Cold Seep Ecosystems. *Oceanography*, *22*(1), 92–109. https://doi.org/10.5670/oceanog.2009.11.
17. Francis, C. A., Roberts, K. J., Beman, J. M., Santoro, A. E., & Oakley, B. B. (2005). Ubiquity and diversity of ammonia-oxidizing archaea in water columns and sediments of the ocean. *Proceedings of the National Academy of Sciences*, *102*(41), 14683–14688. https://doi.org/10.1073/pnas.0506625102.
18. Fuhrman, J. A., McCallum, K. & Davis, A. A. (1992). Novel major Archaebacterial group from marine plankton. *Nature* 356, 148–149. https://doi.org/10.1038/356148a0.
19. Gao, K. (2020). Manipulation of Seawater Carbonate Chemistry. *Research Methods of Environmental Physiology in Aquatic Sciences*, 25–37. https://doi.org/10.1007/978-981-15-5354-7_3.
20. Gudipati, M.S., Henderson, B.L. & Bateman, F.B. (2020). Laboratory predictions for the night-side surface ice glow of Europa. *Nat Astron*. 5, 276–282. https://doi.org/10.1038/s41550-020-01248-1.
21. Gulick, V. C. (2001). Origin of the valley networks on Mars: a hydrological perspective. Geomorphology, 37(3–4), 241–268. https://doi.org/10.1016/s0169-555x(00)00086-6.
22. Hollis, C. J., Taylor, K. W., Handley, L., Pancost, R. D., Huber, M., Creech, J. B., Hines, B. R., Crouch, E. M., Morgans, H. E., Crampton, J. S., Gibbs, S., Pearson, P. N., & Zachos, J. C. (2012). Early Paleogene temperature history of the Southwest Pacific Ocean: Reconciling proxies and models. *Earth and Planetary Science Letters*, *349–350*, 53–66. https://doi.org/10.1016/j.epsl.2012.06.024.
23. Huguet, C., Hopmans, E. C., Febo-Ayala, W., Thompson, D. H., Sinninghe Damsté, J. S., & Schouten, S. (2006). An improved method to determine the absolute abundance of glycerol dibiphytanyl glycerol tetraether lipids. *Organic Geochemistry*, *37*(9), 1036–1041. https://doi.org/10.1016/j.orggeochem.2006.05.008.
24. Hurley, S. J., Close, H. G., Elling, F. J., Jasper, C. E., Gospodinova, K., McNichol, A. P., & Pearson, A. (2019). CO2-dependent carbon isotope fractionation in Archaea, Part II: The marine water column. *Geochimica et Cosmochimica Acta*, *261*, 383–395. https://doi.org/10.1016/j.gca.2019.06.043.

25. Ingalls, A. E., Shah, S. R., Hansman, R. L., Aluwihare, L. I., Santos, G. M., Druffel, E. R. M., & Pearson, A. (2006). Quantifying archaeal community autotrophy in the mesopelagic ocean using natural radiocarbon. *Proceedings of the National Academy of Sciences,* 103(17), 6442–6447. https://doi.org/10.1073/pnas.0510157103.
26. Ijiri, A., Harada, N., Hirota, A., Tsunogai, U., Ogawa, N. O., Itaki, T., Khim, B. K., & Uchida, M. (2012). Biogeochemical processes involving acetate in sub-seafloor sediments from the Bering Sea shelf break. *Organic Geochemistry*, *48*, 47–55. https://doi.org/10.1016/j.orggeochem.2012.04.004.
27. Jenkyns, H. C., Schouten-Huibers, L., Schouten, S., & Sinninghe Damsté, J. S. (2012). Warm Middle Jurassic–Early Cretaceous high-latitude sea-surface temperatures from the Southern Ocean. *Climate of the Past,* 8(1), 215–226. https://doi.org/10.5194/cp-8-215-2012.
28. Joseph, C., Campbell, K. A., Torres, M. E., Martin, R. A., Pohlman, J. W., Riedel, M., & Rose, K. (2013). Methane-derived authigenic carbonates from modern and paleoseeps on the Cascadia margin: Mechanisms of formation and diagenetic signals. *Palaeogeography, Palaeoclimatology, Palaeoecology*, *390*, 52–67. https://doi.org/10.1016/j.palaeo.2013.01.012.
29. Kaneko, M., Shingai, H., Pohlman, J. W., & Naraoka, H. (2010). Chemical and isotopic signature of bulk organic matter and hydrocarbon biomarkers within mid-slope accretionary sediments of the northern Cascadia margin gas hydrate system. *Marine Geology*, *275*(1–4), 166–177. https://doi.org/10.1016/j.margeo.2010.05.010.
30. Kelleyl, C. A., Coffin, R. B., & Cifuentes, L. A. (1998). Stable isotope evidence for alternative bacterial carbon sources in the Gulf of Mexico. *Limnology and Oceanography*, *43*(8), 1962–1969. https://doi.org/10.4319/lo.1998.43.8.1962.
31. Kheshgi, H. S. (1995). Sequestering atmospheric carbon dioxide by increasing ocean alkalinity. *Energy*, *20*(9), 915–922. https://doi.org/10.1016/0360-5442(95)00035-f.
32. Kim, J. H., Schouten, S., Hopmans, E. C., Donner, B., & Sinninghe Damsté, J. S. (2008). Global sediment core-top calibration of the TEX86 paleothermometer in the ocean. *Geochimica et Cosmochimica Acta*, *72*(4), 1154–1173. https://doi.org/10.1016/j.gca.2007.12.010.
33. Kim, J. H., van der Meer, J., Schouten, S., Helmke, P., Willmott, V., Sangiorgi, F., Koç, N., Hopmans, E. C., & Damsté, J. S. S. (2010). New indices and calibrations derived from the distribution of crenarchaeal isoprenoid tetraether lipids: Implications for past sea surface temperature reconstructions. *Geochimica et Cosmochimica Acta*, *74*(16), 4639–4654. https://doi.org/10.1016/j.gca.2010.05.027
34. Knittel, K., & Boetius, A. (2009). Anaerobic Oxidation of Methane: Progress with an Unknown Process. Annual Review of Microbiology, 63(1), 311–334. https://doi.org/10.1146/annurev.micro.61.080706.093130.

35. Koga, Y., Nishihara, M., Morii, H., & Akagawa-Matsushita, M. (1993). Ether polar lipids of methanogenic bacteria: structures, comparative aspects, and biosyntheses. *Microbiological reviews*, *57*(1), 164–182. https://doi.org/10.1128/mr.57.1.164-182.1993.
36. Kozlowski, J. A., Stieglmeier, M., Schleper, C., Klotz, M. G., & Stein, L. Y. (2016). Pathways and key intermediates required for obligate aerobic ammonia-dependent chemolithotrophy in bacteria and Thaumarchaeota. *The ISME Journal*, *10*(8), 1836–1845. https://doi.org/10.1038/ismej.2016.2.
37. Kump, L., Bralower, T., & Ridgwell, A. (2009). Ocean Acidification in Deep Time. *Oceanography*, *22*(4), 94–107. https://doi.org/10.5670/oceanog.2009.100
38. Kurth, J. M., Smit, N. T., Berger, S., Schouten, S., Jetten, M. S. M., & Welte, C. U. (2019). Anaerobic methanotrophic archaea of the ANME-2d clade feature lipid composition that differs from other ANME archaea. *FEMS Microbiology Ecology*, *95*(7), fiz082. https://doi.org/10.1093/femsec/fiz082
39. Kusoglu, A., & Weber, A. Z. (2017). New Insights into Perfluorinated Sulfonic-Acid Ionomers. *Chemical Reviews*, *117*(3), 987–1104. https://doi.org/10.1021/acs.chemrev.6b00159.
40. Lincoln, S. A., Wai, B., Eppley, J. M., Church, M. J., Summons, R. E., & DeLong, E. F. (2014). Planktonic Euryarchaeota are a significant source of archaeal tetraether lipids in the ocean. *Proceedings of the National Academy of Sciences*, *111*(27), 9858–9863. https://doi.org/10.1073/pnas.1409439111.
41. Liu, Z., Pagani, M., Zinniker, D., DeConto, R., Huber, M., Brinkhuis, H., Shah, S. R., Leckie, R. M., & Pearson, A. (2009). Global Cooling During the Eocene-Oligocene Climate Transition. *Science*, *323*(5918), 1187–1190. https://doi.org/10.1126/science.1166368.
42. Lloyd, K. G., Alperin, M. J., & Teske, A. (2011). Environmental evidence for net methane production and oxidation in putative ANaerobic MEthanotrophic (ANME) archaea. *Environmental Microbiology*, *13*(9), 2548–2564. https://doi.org/10.1111/j.1462-2920.2011.02526.x.
43. Lopes Dos Santos, R. A., Spooner, M. I., Barrows, T. T., de Deckker, P., Sinninghe Damsté, J. S., & Schouten, S. (2013). Comparison of organic (UK'37, TEXH86, LDI) and faunal proxies (foraminiferal assemblages) for reconstruction of late Quaternary sea surface temperature variability from offshore southeastern Australia. *Paleoceanography*, *28*(3), 377–387. https://doi.org/10.1002/palo.20035.
44. Macalady, J. L., Vestling, M. M., Baumler, D., Boekelheide, N., Kaspar, C. W., & Banfield, J. F. (2004). Tetraether-linked membrane monolayers in Ferroplasma spp: a key to survival in acid. *Extremophiles*, *8*(5), 411–419. https://doi.org/10.1007/s00792-004-0404-5.
45. Mohr, W., Tang, T., Sattin, S. R., Bovee, R. J., & Pearson, A. (2014). Protein Stable Isotope Fingerprinting: Multidimensional Protein Chromatography Coupled to Stable

Isotope-Ratio Mass Spectrometry. *Analytical Chemistry,* 86(17), 8514–8520. https://doi.org/10.1021/ac502494b.

46. Moreira, D., López-García, P. Symbiosis Between Methanogenic Archaea and δ-Proteobacteria as the Origin of Eukaryotes: The Syntrophic Hypothesis. *J Mol Evol* 47, 517–530 (1998). https://doi.org/10.1007/PL00006408.
47. Omoregie, E. O., Niemann, H., Mastalerz, V., de Lange, G. J., Stadnitskaia, A., Mascle, J., Foucher, J. P., & Boetius, A. (2009). Microbial methane oxidation and sulfate reduction at cold seeps of the deep Eastern Mediterranean Sea. *Marine Geology*, *261*(1–4), 114–127. https://doi.org/10.1016/j.margeo.2009.02.001.
48. Pancost, R., Hopmans, E., & Sinninghe Damsté, J. (2001). Archaeal lipids in Mediterranean cold seeps: molecular proxies for anaerobic methane oxidation. *Geochimica et Cosmochimica Acta*, *65*(10), 1611–1627. https://doi.org/10.1016/s0016-7037(00)00562-7.
49. Parenteau, M. N., Jahnke, L. L., Farmer, J. D., & Cady, S. L. (2014). Production and early preservation of lipid biomarkers in iron hot springs. *Astrobiology*, *14*(6), 502–521. https://doi.org/10.1089/ast.2013.1122.
50. Pearson, A., & Ingalls, A. E. (2013). Assessing the Use of Archaeal Lipids as Marine Environmental Proxies. *Annual Review of Earth and Planetary Sciences*, *41*(1), 359–384. https://doi.org/10.1146/annurev-earth-050212-123947.
51. Pearson, A., Hurley, S. J., Walter, S. R. S., Kusch, S., Lichtin, S., & Zhang, Y. G. (2016). Stable carbon isotope ratios of intact GDGTs indicate heterogeneous sources to marine sediments. *Geochimica et Cosmochimica Acta*, *181*, 18–35. https://doi.org/10.1016/j.gca.2016.02.034.
52. Pester M, Schleper C, Wagner M. The Thaumarchaeota: an emerging view of their phylogeny and ecophysiology. *Curr Opin Microbiol*. 2011;14(3):300-306. doi:10.1016/j.mib.2011.04.007.
53. Pohlman, J.W. The biogeochemistry of anchialine caves: progress and possibilities. *Hydrobiologia* 677, 33–51 (2011). https://doi.org/10.1007/s10750-011-0624-5.
54. Reeburgh, W. S. (1976). Methane consumption in Cariaco Trench waters and sediments. *Earth and Planetary Science Letters*, *28*(3), 337–344. https://doi.org/10.1016/0012-821x(76)90195-3.
55. Rothschild, L. J., & Mancinelli, R. L. (2001). Life in extreme environments. *Nature*, *409*(6823), 1092–1101. https://doi.org/10.1038/35059215.
56. Russell, M. J., Murray, A. E., & Hand, K. P. (2017). The Possible Emergence of Life and Differentiation of a Shallow Biosphere on Irradiated Icy Worlds: The Example of Europa. *Astrobiology*, *17*(12), 1265–1273. https://doi.org/10.1089/ast.2016.1600.
57. Schmittner, A., Gruber, N., Mix, A. C., Key, R. M., Tagliabue, A., & Westberry, T. K. (2013). Biology and air–sea gas exchange controls on the distribution of carbon isotope ratios ($\delta^{13}C$) in the ocean. *Biogeosciences*, *10*(9), 5793–5816. https://doi.org/10.5194/bg-10-5793-2013.

58. Schouten, S., Hopmans, E. C., Pancost, R. D., & Damste, J. S. S. (2000). Widespread occurrence of structurally diverse tetraether membrane lipids: Evidence for the ubiquitous presence of low-temperature relatives of hyperthermophiles. *Proceedings of the National Academy of Sciences,* 97(26), 14421–14426. https://doi.org/10.1073/pnas.97.26.14421.
59. Schouten, S., Hopmans, E. C., Schefuß, E., & Sinninghe Damsté, J. S. (2002). Distributional variations in marine crenarchaeotal membrane lipids: a new tool for reconstructing ancient sea water temperatures? *Earth and Planetary Science Letters*, *204*(1–2), 265–274. https://doi.org/10.1016/s0012-821x(02)00979-2.
60. Schouten, S., van der Meer, M. T. J., Hopmans, E. C., Rijpstra, W. I. C., Reysenbach, A. L., Ward, D. M., & Sinninghe Damsté, J. S. (2007). Archaeal and Bacterial Glycerol Dialkyl Glycerol Tetraether Lipids in Hot Springs of Yellowstone National Park. *Applied and Environmental Microbiology,* 73(19), 6181–6191. https://doi.org/10.1128/aem.00630-07.
61. Schouten, S., Hopmans, E. C., & Sinninghe Damsté, J. S. (2013). The organic geochemistry of glycerol dialkyl glycerol tetraether lipids: A review. *Organic Geochemistry*, *54*, 19–61. https://doi.org/10.1016/j.orggeochem.2012.09.006.
62. Sessions, A. L., Sylva, S. P., & Hayes, J. M. (2005). Moving-Wire Device for Carbon Isotopic Analyses of Nanogram Quantities of Nonvolatile Organic Carbon. *Analytical Chemistry*, *77*(20), 6519–6527. https://doi.org/10.1021/ac051251z.
63. Shah, S. R., & Pearson, A. (2007). Ultra-Microscale (5–25 μg C) Analysis of Individual Lipids by 14C AMS: Assessment and Correction for Sample Processing Blanks. *Radiocarbon*, *49*(1), 69–82. https://doi.org/10.1017/s0033822200041904.
64. Shah, S. R., Mollenhauer, G., Ohkouchi, N., Eglinton, T. I., & Pearson, A. (2008). Origins of archaeal tetraether lipids in sediments: Insights from radiocarbon analysis. *Geochimica et Cosmochimica Acta*, *72*(18), 4577–4594. https://doi.org/10.1016/j.gca.2008.06.021.
65. Silvera, K., Santiago, L., Cushman, J.C., Winter, K. (2010). The incidence of crassulacean acid metabolism in Orchidaceae derived from carbon isotope ratios: a checklist of the flora of Panama and Costa Rica. *Botanical Journal of the Linnean Society*, *163*(2), 194–222. https://doi.org/10.1111/j.1095-8339.2010.01058.x
66. Spence, W. (1989). Stress origins and earthquake potentials in Cascadia. *Journal of Geophysical Research: Solid Earth*, *94*(B3), 3076–3088. https://doi.org/10.1029/jb094ib03p03076.
67. Stadnitskaia, A., Nadezhkin, D., Abbas, B., Blinova, V., Ivanov, M., & Sinninghe Damsté, J. (2008). Carbonate formation by anaerobic oxidation of methane: Evidence from lipid biomarker and fossil 16S rDNA. *Geochimica et Cosmochimica Acta*, *72*(7), 1824–1836. https://doi.org/10.1016/j.gca.2008.01.020.
68. Stahl, D. A., & de la Torre, J. R. (2012). Physiology and Diversity of Ammonia-Oxidizing Archaea. *Annual Review of Microbiology*, *66*(1), 83–101. https://doi.org/10.1146/annurev-micro-092611-150128.

69. Tierney, J. E., Oppo, D. W., Rosenthal, Y., Russell, J. M., & Linsley, B. K. (2010). Coordinated hydrological regimes in the Indo-Pacific region during the past two millennia. *Paleoceanography*, *25*(1). https://doi.org/10.1029/2009pa001871.
70. Tierney, J. E., & Tingley, M. P. (2014). A Bayesian, spatially-varying calibration model for the TEX_{86} proxy. *Geochimica et Cosmochimica Acta*, *127*, 83–106. https://doi.org/10.1016/j.gca.2013.11.026.
71. Tierney, J. E., & Tingley, M. P. (2015). A TEX86 surface sediment database and extended Bayesian calibration. Scientific Data, 2(1). https://doi.org/10.1038/sdata.2015.29.
72. Valentine D.L. (2007) Adaptations to energy stress dictate the ecology and evolution of the Archaea. *Nature Rev. Microbiol.* 5, 316–323. https://doi.org/10.1038/nrmicro1619.
73. Wakeham, S. G., Lewis, C. M., Hopmans, E. C., Schouten, S., & Sinninghe Damsté, J. S. (2003). Archaea mediate anaerobic oxidation of methane in deep euxinic waters of the Black Sea. *Geochimica et Cosmochimica Acta*, *67*(7), 1359–1374. https://doi.org/10.1016/s0016-7037(02)01220-6
74. Wakeham, S. G., Hopmans, E. C., Schouten, S., & Sinninghe Damsté, J. S. (2004). Archaeal lipids and anaerobic oxidation of methane in euxinic water columns: a comparative study of the Black Sea and Cariaco Basin. *Chemical Geology*, *205*(3–4), 427–442. https://doi.org/10.1016/j.chemgeo.2003.12.024
75. Weijers, J. W. H., Schouten, S., Hopmans, E. C., Geenevasen, J. A. J., David, O. R. P., Coleman, J. M., Pancost, R. D., & Sinninghe Damste, J. S. (2006). Membrane lipids of mesophilic anaerobic bacteria thriving in peats have typical archaeal traits. *Environmental Microbiology,* 8(4), 648–657. https://doi.org/10.1111/j.1462-2920.2005.00941.x.
76. Wilhelm, M. B., Davila, A. F., Eigenbrode, J. L., Parenteau, M. N., Jahnke, L. L., Liu, X. L., Summons, R. E., Wray, J. J., Stamos, B. N., O'Reilly, S. S., & Williams, A. (2017). Xeropreservation of functionalized lipid biomarkers in hyperarid soils in the Atacama Desert. *Organic geochemistry*, *103*, 97–104. https://doi.org/10.1016/j.orggeochem.2016.10.015.
77. Woese, C. R., Magrum, L. J. & Fox, G. E. (1978). Archaebacteria. J. *Mol. Evol.* 11, 245–252. https://doi.org/10.1007/BF01734485.
78. Wuchter, C., Schouten, S., Coolen, M. J. L., & Sinninghe Damsté, J. S. (2004). Temperature-dependent variation in the distribution of tetraether membrane lipids of marine Crenarchaeota: Implications for TEX86paleothermometry. *Paleoceanography*, *19*(4), n/a. https://doi.org/10.1029/2004pa001041
79. Yuen, G., Blair, N., Des Marais, D. *et al.* Carbon isotope composition of low molecular weight hydrocarbons and monocarboxylic acids from Murchison meteorite. *Nature* 307, 252–254 (1984). https://doi.org/10.1038/307252a0.
80. Zhang, Y. G., Zhang, C. L., Liu, X. L., Li, L., Hinrichs, K. U., & Noakes, J. E. (2011). Methane Index: A tetraether archaeal lipid biomarker indicator for detecting the

instability of marine gas hydrates. *Earth and Planetary Science Letters*, *307*(3–4), 525–534. https://doi.org/10.1016/j.epsl.2011.05.031

81. Zoltov, M. Y., and Shock, E. L. (2000). An abiotic origin for hydrocarbons in the Allan Hills 84001 martian meteorite through cooling of magmatic and impact-generated gases. Meteoritics & Planetary Science, 35(3), 629–638. https://doi.org/10.1111/j.1945-5100.2000.tb01443.x.